fluids

MDPI

Article

CFD and CHT Methodology for the Thermal Simulation and Validation of a Prismatic $LiFePO_4$ Cell

Duccio Fedeli [1], Marco Lagnoni [1], Claudio Scarpelli [2], Francesco Giuseppe Quilici [2], Antonio Bertei [1], Giovanni Lutzemberger [2], Filippo Fruzza [1], Maria Vittoria Salvetti [1,*] and Alessandro Mariotti [1]

[1] Dipartimento di Ingegneria Civile e Industriale, Università di Pisa, 56122 Pisa, Italy; duccio.fedeli@phd.unipi.it (D.F.); marco.lagnoni@unipi.it (M.L.); antonio.bertei@unipi.it (A.B.); filippo.fruzza@ing.unipi.it (F.F.); alessandro.mariotti@unipi.it (A.M.)

[2] Dipartimento di Ingegneria dell'Energia, dei Sistemi, del Territorio e delle Costruzioni, Università di Pisa, 56122 Pisa, Italy; claudio.scarpelli@unipi.it (C.S.); francesco.quilici@phd.unipi.it (F.G.Q.); giovanni.lutzemberger@unipi.it (G.L.)

* Correspondence: maria.vittoria.salvetti@unipi.it

Abstract

A computational fluid dynamics and conjugate heat transfer (CFD+CHT) methodology is developed for the thermal simulation of a commercial prismatic $LiFePO_4$ cell under charging and discharging operating conditions. The approach couples a three-dimensional representation of the battery, including a simplified description of its internal layered structure, with an electrochemical–thermal heat-generation model implemented as a temperature- and time-dependent volumetric source term. The heat source is applied within the active layers of the cell and updated during the transient simulation according to the local thermal state and to the evolution of the state of charge. The methodology is applied to 1C and 2C cycles under natural convection and forced-air cooling at free-stream velocities of 10 m s^{-1} and 20 m s^{-1}. A dedicated wind-tunnel campaign is carried out on the same cell, instrumented with type-K thermocouples distributed over its external surfaces, to provide experimental data for model validation. The results show that the proposed framework accurately reproduces the main wall-temperature trends observed experimentally. Under natural convection, the temperature distribution remains nearly uniform, whereas forced convection produces more pronounced vertical and in-plane gradients. For the charge cycles, the comparison between CFD predictions and end-of-cycle measurements yields a mean absolute error (MAE) of 0.66 °C and a root-mean-square error (RMSE) of 0.82 °C over 168 measurement locations. The discharge cycles yield a comparable level of agreement (MAE 0.65 °C, RMSE 0.81 °C over 168 probe points), confirming the predictive capability of the methodology for both operating modes.

Keywords: lithium-ion battery; $LiFePO_4$ cell; battery thermal management; conjugate heat transfer; computational fluid dynamics; experimental validation

Academic Editor: Kambiz Vafai

Received: 18 June 2026
Revised: 15 August 2026
Accepted: 16 August 2026
Published: 18 August 2026

1. Introduction

The transition towards electric mobility is placing rechargeable batteries at the centre of automotive research and development. In battery electric vehicles (BEVs), the battery pack is not only the primary onboard energy storage system but also one of the components that most strongly influences vehicle safety, durability, efficiency, charging performance, and overall operating cost. Among the available electrochemical energy storage technologies, lithium-ion batteries currently represent the leading solution for automotive

applications owing to their high energy density, high power capability, low self-discharge rate, and long cycle life. However, their performance and degradation behaviour are strongly influenced by the operating temperature. Excessively high temperatures accelerate ageing mechanisms and may lead to safety-critical conditions, whereas low temperatures reduce power capability, charging efficiency, and available capacity [1,2].

Maintaining lithium-ion batteries within a controlled temperature range is therefore essential to preserve performance, safety, and lifetime. In addition to limiting the maximum cell temperature, an effective Battery Thermal Management System (BTMS) must minimise thermal non-uniformities within the cell, module, and pack, since local hot spots and large temperature gradients can accelerate degradation, impair electrochemical performance, and increase the risk of thermal runaway. This requirement becomes particularly relevant under demanding operating conditions, such as high C-rate cycling, fast charging, and operation under extreme ambient temperatures. For this reason, recent studies have focused on the development and comparison of different thermal-management strategies aimed at improving heat dissipation and temperature uniformity in electric-vehicle battery packs [3–7].

Several thermal management strategies have been proposed in the literature, including air cooling, liquid cooling, phase-change-material-based systems, thermoelectric systems, and hybrid solutions [8,9]. Air cooling is attractive because of its simplicity, low cost, and ease of integration, but it usually provides a lower heat-transfer capability and may lead to non-uniform temperature distributions. Liquid cooling generally offers higher thermal performance and better temperature control, at the price of increased system complexity, weight, and integration constraints. The selection and optimisation of a BTMS therefore require numerical tools able to predict not only the maximum temperature of the cell, but also the spatial distribution of temperature and the effect of the cooling flow.

Battery thermal modelling is challenging because several coupled physical phenomena occur simultaneously. Heat is generated inside the electrochemical cell as a consequence of irreversible losses and reversible entropic effects, while heat is transported through the anisotropic layered structure of the battery and finally exchanged with the surrounding fluid by convection. The classical energy balance proposed by Bernardi et al. [10] provides a fundamental framework for estimating heat generation in electrochemical systems. Since then, different modelling approaches have been developed, ranging from lumped thermal models and equivalent-circuit electro-thermal models to physics-based electrochemical models and fully three-dimensional computational fluid dynamics (CFD)/conjugate heat transfer (CHT) simulations [11–13].

Besides the external heat-removal mechanism, the prediction of battery thermal behaviour requires a suitable description of the internal electrochemical heat-generation process. Full-order electrochemical models based on porous electrode theory can provide detailed information on the internal state of the cell, but their computational cost may become prohibitive when they are coupled with three-dimensional thermal or CFD simulations. For this reason, several reduced-order approaches have been proposed, including control-oriented electrochemical models, single-particle models, equivalent-circuit models, and model-order-reduction strategies for diffusion-dominated battery dynamics. These models provide a practical compromise between physical consistency and computational efficiency, making them suitable for coupling with CFD+CHT simulations through a time- and temperature-dependent volumetric heat source [14–18].

Reduced-order and equivalent-circuit models are computationally efficient and well suited for control-oriented applications and battery management systems. Their spatial resolution is limited: they cannot directly describe the local interaction between the battery surface and the external cooling flow. Three-dimensional CFD and CHT simulations

solve the conductive heat transfer in the solid and the convective heat transfer in the fluid consistently, providing detailed information on wall-temperature gradients, hot-spot formation, and cooling-flow efficiency. The main limitation is computational cost, which grows rapidly when the analysis is extended from a single cell to battery modules or full packs, and which may restrict direct use in real-time monitoring or many-query design procedures. A validated CFD+CHT model can serve as the high-fidelity physical basis from which reduced or data-augmented models are derived for future monitoring and optimisation of the BTMS [19–21].

A further difficulty is associated with the internal structure of prismatic lithium-ion cells. The cell is composed of a large number of thin layers, including current collectors, electrodes, separator, tabs, and external casing. This structure makes the thermal behaviour anisotropic, since heat conduction along the electrode and collector planes differs from heat conduction through the cell thickness. A fully resolved geometrical representation of all internal layers would be prohibitively expensive for a CFD+CHT analysis intended to be extended to larger assemblies. Therefore, an effective methodology should preserve the main thermal features of the real layered architecture while keeping the computational cost compatible with engineering design workflows.

Several CFD-based and electro-thermal methodologies have been proposed to address these issues at different levels of detail. Panchal et al. [22] developed a transient electrochemical heat-transfer model for a large-format prismatic $LiFePO_4$/graphite cell and validated it experimentally under different C-rates, highlighting the importance of transient heat-generation modelling for predicting the thermal response of LFP cells. At module level, Wang et al. [23] investigated the influence of cell arrangement and forced-air-cooling strategies by means of three-dimensional CFD simulations, showing how the airflow configuration strongly affects both the maximum temperature and the temperature uniformity within the module. Chen et al. [24] compared different cooling concepts, including air cooling, direct liquid cooling, indirect liquid cooling, and fin-based cooling, using an electrochemical–thermal framework to assess the trade-off between cooling performance, temperature uniformity, parasitic power consumption, and additional system weight. Other studies have focused on detailed thermal characterisation and model validation for prismatic cells. For instance, Kleiner et al. [13] developed and experimentally validated a three-dimensional electro-thermal model of a prismatic lithium-ion cell under BEV-relevant boundary conditions, while Akbarzadeh et al. [25] proposed a thermal characterisation methodology for identifying heat capacity and anisotropic thermal conductivity and applied it to both cell- and module-level simulations. More recently, CFD+CHT approaches have also been adopted in safety-oriented studies, such as the work of Kong et al. [26], where conjugate heat transfer and CFD were coupled to investigate thermal runaway evolution and jet fire in cylindrical 18650 cells under abuse conditions.

Despite these advances, most existing CFD+CHT frameworks for battery thermal simulations rely on simplified electrochemical heat-generation formulations, typically equivalent-circuit or lumped Bernardi-type models, that limit the physical fidelity of the predicted heat-generation profile, particularly at high C-rates and over a broad temperature range. The coupling of a physics-based electrochemical model, capable of resolving the individual contributions of reversible entropy effects, reaction overpotentials, and ohmic dissipation, with a three-dimensional CFD+CHT solver has received limited attention in the literature. Furthermore, most validation studies compare CFD results with experimental data obtained from separate setups, whereas dedicated campaigns in which the numerical and experimental configurations are designed to match one another point by point remain relatively uncommon.

Within this context, the present work develops a CFD+CHT methodology for the thermal simulation and experimental validation of a commercial prismatic $LiFePO_4$ cell. The main contributions of the present work are threefold: (i) the integration of the Pseudo-2-Dimensional (P2D) electrochemical–thermal model of Lagnoni et al. [27] into a three-dimensional CFD+CHT solver. The physics-based heat-generation rate is pre-computed, tabulated as a function of time and temperature, and applied as a volumetric source term updated at each thermal time step. The model is adopted without modifications and without any parameter adjustment to match the present measurements; (ii) a sensitivity analysis of the internal layered representation of the prismatic cell, leading to the identification of effective in-plane and through-plane thermal conductivity values for the simplified geometry; and (iii) a dedicated wind-tunnel experimental campaign performed on the same cell and under the same aerodynamic configuration considered in the numerical model, enabling a direct point-by-point comparison between measured and simulated wall temperatures.

The objective of this work is to develop a physically consistent yet computationally efficient tool for predicting the wall-temperature evolution of a cell under different operating conditions. Natural convection and forced-air cooling are investigated for 1C and 2C charge and discharge cycles. The proposed approach represents a first step toward a scalable methodology for the thermal analysis of battery modules and full battery packs, where the accurate prediction of local temperature gradients is essential for the design and optimisation of effective BTMS solutions.

2. Test Case

The test case considered in this work is a commercial ZG-LFP060AH prismatic lithium iron phosphate ($LiFePO_4$) cell, shown in Figure 1a. The cell has a nominal capacity of 60 Ah, a nominal voltage of 3.2 V, and external dimensions equal to 130 mm $\times$ 186 mm $\times$ 36 mm (width, height, and thickness, respectively). The corresponding mass is approximately 1.685 kg. The main electrical and geometrical specifications are provided by the manufacturer datasheet [28]. The selected cell is representative of large-format prismatic LFP batteries used in automotive and stationary energy-storage applications, where thermal management is required to preserve performance, safety, and lifetime.

This cell has already been tested in a climatic chamber by Barbieri et al. [29], providing a thermal reference dataset for the selected cell. The choice of this specific cell is also motivated by the availability of a dedicated electrochemical–thermal heat-generation model developed for the same 60 Ah graphite/$LiFePO_4$ prismatic cell by Lagnoni et al. [27]. The model provides the cell heat generation as a function of the operating condition, including state of charge and temperature. This feature makes it particularly suitable for coupling with CFD+CHT simulations, since the internal heat production can be introduced in the energy equation as a time- and temperature-dependent volumetric source term. The implementation of this model within the numerical methodology is described in detail in Section 3.1.

From a fluid-dynamic point of view, the prismatic geometry of the cell plays a central role in the definition of the test case. In the wind-tunnel configuration considered in this work, the incoming airflow impinges on the cell, which behaves as an isolated bluff body. Owing to its sharp edges and finite thickness, the flow separates around the battery and develops a wake downstream of the cell. This wake is characterised by recirculation regions and large-scale unsteady structures, which affect the local convective heat transfer at the cell surface.

The aerodynamic time scales associated with flow separation and wake development are much shorter than the thermal time scales governing the temperature evolution of

the battery during a charge or discharge cycle. The thermal response of the cell is mainly driven by internal heat generation, solid conduction through the layered structure, and convective exchange at the external surfaces. As a result, the wall temperature evolves gradually over the duration of the operating cycle, whereas the external flow may exhibit faster unsteady fluctuations. Directly resolving both phenomena throughout the entire battery cycle would significantly increase the computational cost of the simulation.

For this reason, the test-case configuration includes a flat plate positioned downstream of the battery, as shown in Figure 1b. The plate is aligned with the incoming flow and is designed to limit the development of large-scale wake oscillations behind the cell. Its purpose is to promote a quasi-steady recirculation pattern in the near wake and to obtain a more stable velocity field around the battery. The same configuration is adopted in both the numerical simulations and the experimental campaign, so as to ensure consistency between CFD predictions and wind-tunnel measurements.

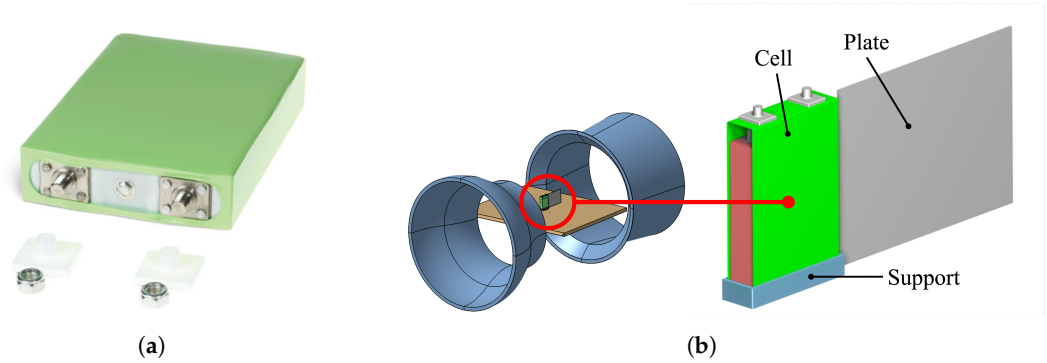

Figure 1. Test case setup: battery cell and wind-tunnel configuration. (**a**) ZG-LFP060AH prismatic lithium iron phosphate cell. (**b**) Wind-tunnel configuration.

The resulting geometry, together with the symbols used for the characteristic dimensions of the cell and of the splitter plate, is defined in Figure 2. The plate has a length of $L_{sp} = 210$ mm and a height equal to that of the battery. Taking the battery thickness $D^* = 36$ mm as the reference dimension, the length ratio is $L_{sp}/D^* \approx 5.8$. This value was selected on the basis of published studies on splitter-plate effectiveness for finite bluff bodies with comparable geometry. For finite circular cylinders of aspect ratio $AR \approx 5$, vortex-shedding suppression is achieved for $L/D \gtrsim 1.5$ [30], while for finite rectangular prisms, a similar threshold applies [31]. The prismatic battery has a cross-sectional depth ratio $CR = B/D^* \approx 3.6$ (where $B = 130$ mm is the cell width), a range in which the impinging-shear-layer instability of the separated flow promotes unsteady reattachment on the rear face [32,33]. The selected $L_{sp}/D^* \approx 5.8$ is therefore a conservative choice that ensures robust shedding suppression across all tested velocities.

The operating conditions investigated in the present work are summarised in Table 1. Two C-rates, 1C and 2C, are considered for both charge and discharge, and each electrical condition is combined with the three cooling configurations, namely natural convection and forced convection at 10 and 20 m s^{-1}, for a total of twelve cases.

Once the external flow field has reached a stabilised condition, the subsequent thermal transient is computed by activating the internal heat-generation term inside the battery. In this way, the convective heat transfer is evaluated on the basis of a nearly stationary aerodynamic field, while the temperature field evolves according to the coupled conductive–convective heat-transfer mechanisms. This strategy reduces the computational cost while retaining the main physical interaction between external cooling and internal heat generation. The numerical details of the CFD+CHT implementation are reported in Section 3.3.

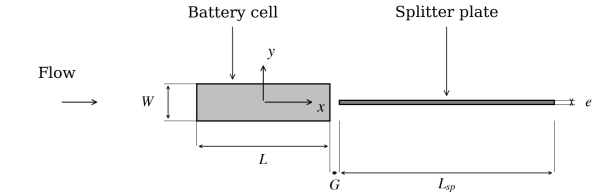

(**a**)

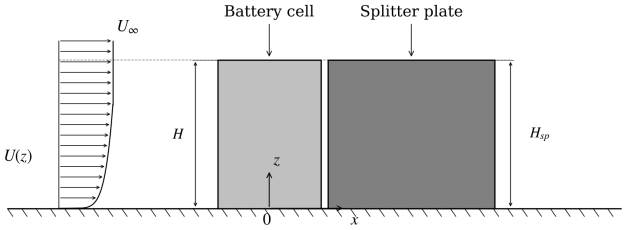

(**b**)

Figure 2. Schematic of the battery cell and splitter-plate configuration. (**a**) Top view: L, W: streamwise length and spanwise width of the cell body; G: gap between the cell trailing edge and the splitter-plate leading edge; L_{sp}, e: streamwise length and thickness of the splitter plate. (**b**) Side view: H: height of the cell body; H_{sp}: height of the splitter plate; U_∞: free-stream velocity.

Table 1. Test matrix adopted for the CFD+CHT simulations and wind-tunnel validation. Each electrical condition was combined with the three cooling configurations.

Mode	C-Rate	Airflow	Duration
Charge	1C	Natural, 10, 20 m s^{-1}	60 min
Charge	2C	Natural, 10, 20 m s^{-1}	30 min
Discharge	1C	Natural, 10, 20 m s^{-1}	60 min
Discharge	2C	Natural, 10, 20 m s^{-1}	30 min

3. Numerical Methodology

The proposed methodology couples an electrochemical–thermal heat-generation model with a three-dimensional CFD+CHT description of the battery and of the surrounding cooling flow. The objective is to reproduce the transient thermal response of the cell during charge and discharge cycles while maintaining a computational cost compatible with future extensions to battery modules and packs.

The methodology is based on three coupled components. First, the electrochemical–thermal model provides the heat-generation rate as a function of time, state of charge, and temperature. Second, the internal structure of the prismatic cell is represented through a simplified but physically consistent layered geometry, able to reproduce the main anisotropic thermal behaviour of the real cell. Third, the resulting solid model is coupled with the external fluid domain through conjugate heat transfer simulations. The same numerical configuration is then reproduced experimentally in the wind tunnel, allowing a direct point-by-point comparison between computed and measured wall temperatures.

3.1. Electrochemical Model

The internal heat source adopted in the CFD+CHT simulations is derived from the Pseudo-2-Dimensional (P2D) electrochemical–thermal model proposed by Lagnoni et al. [27] for a 60 Ah prismatic graphite/$LiFePO_4$ cell. The P2D framework, originally introduced by Doyle, Fuller, and Newman, is based on porous electrode theory and provides a macroscale homogeneous description of charge and mass conservation in both the solid electrode

phase and the liquid electrolyte phase [27]. The model parameters were calibrated against dedicated electrical characterisation tests reported in Lagnoni et al. [27] and are used here in a fully predictive fashion, without any adjustment to the wind-tunnel measurements. The reader is referred to Lagnoni et al. [27] for the complete governing equations and parametrisation procedure.

The state of charge SOC is the normalised available charge of the cell, with $SOC = 1$ corresponding to the fully charged condition and $SOC = 0$ to the fully discharged condition. It is updated from the imposed current according to

$$SOC(t) = SOC(t_0) - \frac{1}{C_{\text{nom}}} \int_{t_0}^{t} I(t')\, \mathrm{d}t', \tag{1}$$

where C_{nom} is the nominal capacity of the cell. The current I is taken as positive during discharge and negative during charge. With this convention, Equation (1) yields a decreasing SOC during discharge and an increasing SOC during charge, so that the same definition applies to both charge and discharge tests. This sign convention is adopted consistently throughout the manuscript and in the numerical implementation of the heat-generation model.

The C-rate is the current normalised by the nominal capacity and is defined as

$$C\text{-rate} = \frac{|I|}{C_{\text{nom}}}, \tag{2}$$

so that a 1C cycle corresponds to a current that would ideally charge or discharge the cell in one hour, while a 2C cycle corresponds to a nominal cycle duration of thirty minutes. The corresponding evolution of the terminal voltage during a representative 2C charging cycle, as predicted by the P2D model, is shown in Figure 3a.

The total heat generated per unit cell is obtained as the thickness-averaged sum of three physical contributions resolved by the P2D model: the reversible (entropic) heat $\dot{Q}_{\text{rev}}$ associated with electrochemical reaction entropy changes, the irreversible reaction heat $\dot{Q}_{\text{rxn}}$ related to activation overpotentials at the electrode-electrolyte interface, and the ohmic dissipation $\dot{Q}_{\text{ohm}}$ in both the solid and electrolyte phases,

$$\dot{Q} = \frac{1}{L_{\text{tot}}} \int_{0}^{L_{\text{tot}}} (\dot{Q}_{\text{rev}} + \dot{Q}_{\text{rxn}} + \dot{Q}_{\text{ohm}})\, \mathrm{d}x, \tag{3}$$

where $L_{\text{tot}} = L_N + L_S + L_P$ is the total active thickness spanning the negative electrode, separator, and positive electrode. All three contributions depend on the instantaneous electrochemical state and on the local cell temperature. In the present implementation, the P2D model is solved in COMSOL 6.3 for a representative set of temperature values, and the resulting heat-generation law is tabulated as a function of time and temperature. This lookup table is then interpolated during the CFD+CHT calculation to provide the instantaneous heat source at each thermal time step, as illustrated in Figure 3b.

The heat source is introduced in the CFD solver as a volumetric source term applied only to the active layers of the battery. For each computational cell belonging to the active material, the source term is computed as

$$\dot{q}_v(\mathbf{x}, t) = \frac{\dot{Q}(T(\mathbf{x}, t), t)}{V_{\text{act}}}, \tag{4}$$

where V_{act} is the total active volume of the modelled cell. At each thermal time step, the local temperature is read from the CFD solution, the corresponding heat-generation value is evaluated through interpolation, and the volumetric source term is updated. This procedure allows the heat production to depend on both the instantaneous charge state

and the local thermal state of the cell, while avoiding the computational cost of an online electrochemical simulation coupled to the CFD solver.

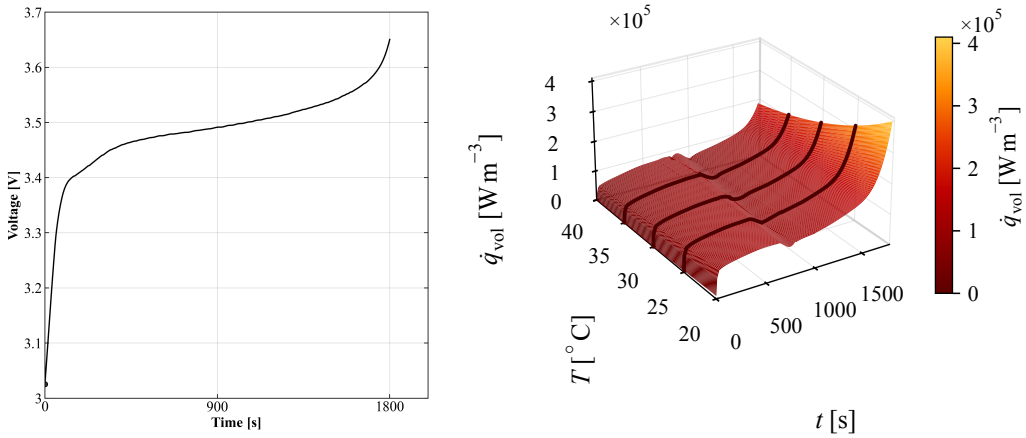

(a) (b)

Figure 3. Output of the P2D electrochemical model for a 2C charging cycle: (**a**) terminal voltage as a function of normalised time; (**b**) volumetric heat-generation rate as a function of cell temperature and time.

3.2. Internal Layering

The internal structure of a prismatic LFP cell consists of a periodic stack of electrochemical layers. Each repeating unit comprises a negative electrode (graphite), a microporous polymeric separator, and a positive electrode (LFP), sandwiched between metallic current collectors [34]. This layered arrangement is the physical origin of the pronounced thermal anisotropy exhibited by lithium-ion prismatic cells. Although the metallic current collectors—aluminium ($\kappa \approx 205$ W m^{-1}K^{-1}) and copper ($\kappa \approx 398$ W m^{-1}K^{-1})—possess high intrinsic thermal conductivity, their individual thicknesses (15–20 µm for Al, 6–10 µm for Cu) are small compared to those of the active electrode coatings (65–100 µm per side). As a result, their contribution to the layer-averaged equivalent conductivity remains limited, particularly in the through-plane direction, which is dominated by the low-conductivity separator and porous electrode coatings.

Explicitly resolving every individual sublayer of the jelly-roll stack in a finite-volume CFD discretisation would require a mesh cell count disproportionate to the scope of the present thermal study: a full-scale prismatic cell may contain on the order of tens to hundreds of repeating units, and resolving each metallic and electrochemical sublayer individually would impose prohibitive memory and runtime costs without commensurate benefit for the cell-level thermal field of interest.

To overcome this limitation, the active volume of the cell is represented through a homogenisation strategy in which the real sublayer sequence is replaced by an alternating stack of two fictitious, homogenised layer types: *active layers* and *passive layers*. Each fictitious layer is assigned an equivalent anisotropic thermal conductivity, computed analytically from the thickness and conductivity of the real sublayers it replaces, so that the resulting reduced-order stack reproduces the same overall thermal resistance—and therefore the same anisotropic heat distribution—as the original layered structure, while drastically reducing the number of mesh elements required. Figure 4 sketches the real sublayer sequence, at true thickness scale, together with its grouping into the two fictitious layer types.

The thickness, density, specific heat capacity and thermal conductivity of the real sublayers used in the homogenisation are collected in Table 2. The equivalent

anisotropic conductivities of the fictitious layers are obtained from the classical thickness-weighted resistance models: the in-plane (parallel) conductivity is the thickness-weighted arithmetic mean

$$k_{\parallel} = \frac{\sum_i k_i t_i}{\sum_i t_i},$$

while the through-plane (series) conductivity is the thickness-weighted harmonic mean

$$k_{\perp} = \frac{\sum_i t_i}{\sum_i t_i / k_i},$$

where t_i and k_i are the thickness and the thermal conductivity of the i-th real sublayer replaced by the fictitious layer.

Table 2. Thickness t, density ρ, specific heat capacity c_p and thermal conductivity k of the real sublayers of the prismatic LFP cell, used to compute the equivalent anisotropic properties of the active and passive fictitious layers.

Layer (Material)	t (µm)	ρ ($\mathrm{kg\,m^{-3}}$)	c_p ($\mathrm{J\,kg^{-1}K^{-1}}$)	k ($\mathrm{W\,m^{-1}K^{-1}}$)
Cu current collector	6–10	8933	385	398
Negative electrode (graphite)	65–90	2200	1100	1.04
Separator (PE/PP)	12–20	1200	1978	0.33
Positive electrode (LFP)	70–100	2500	1100	1.48
Al current collector	15–20	2702	903	205

Active layers incorporate the metallic current collectors together with the adjacent electrode coatings and separator, following the sequence: copper current collector, negative electrode, separator, positive electrode, and aluminium current collector. They are the sites of volumetric heat generation during charge/discharge cycling. Their equivalent thermal conductivity is anisotropic and was computed from the layer thicknesses and constituent material properties: the in-plane conductivity, obtained from a thickness-weighted parallel thermal-resistance model, is $k_{\parallel} = 10\ \mathrm{W\,m^{-1}K^{-1}}$, the thin but highly conductive Cu and Al current collectors dominating the parallel sum.

Passive layers comprise only the electrochemically active materials—negative electrode, separator, and positive electrode—without metallic conductors, and represent the bulk of the jelly-roll volume between two consecutive active layers. No heat generation is assigned to passive layers; they act solely as a conductive medium through which heat generated in the active layers diffuses towards the cell's external boundary. Removing the metallic current collectors suppresses the dominant contribution to in-plane conduction, yielding $k_{\parallel} = 1\ \mathrm{W\,m^{-1}K^{-1}}$, while the through-plane conductivity, already governed in both layer types by the low-conductivity separator and porous electrode coatings, remains $k_{\perp} = 0.1\ \mathrm{W\,m^{-1}K^{-1}}$.

The through-plane value $k_{\perp} = 0.1\ \mathrm{W\,m^{-1}K^{-1}}$, common to both layer types, is adopted as a deliberately conservative lower bound rather than as a best estimate of the physical conductivity, and it is worth stating explicitly on what basis. Dedicated thermal-characterisation measurements on prismatic and large-format cells report through-plane conductivities about one order of magnitude higher than the value adopted here [25,35], and the series model applied to the nominal sublayer properties of Table 2 gives the same order of magnitude. The values collected in the literature are, however, widely dispersed, and surveys of the thermal parameters adopted in thermoelectrochemical models report through-plane conductivities as low as the one used here [36]. Both estimates, however, rest on nominal material properties and on an ideally bonded stack. They do not account for the electrolyte-filled porosity of the coatings and of the separator, nor for the thermal contact

resistances at the numerous electrode/separator/current-collector interfaces of the wound structure, which dominate cross-layer conduction in a real cell; the experimentally observed dependence of the through-plane conductivity on the external compression pressure [35] is a direct signature of the role played by these interfaces. The value adopted here therefore lies at the lower end of the range reported in the literature, and is retained as a conservative choice. Adopting this lower bound results in a reduced effective through-plane thermal diffusivity, thereby producing a conservative overestimate of the internal through-thickness temperature gradients—the prudent direction for the thermal-management and safety assessment pursued in this work.

Nevertheless, the uncertainty associated with the effective through-plane conductivity remains a limitation of the present model. Variations in $k_{\perp}$ may affect the internal-to-surface thermal resistance, the transient wall-temperature response, and the redistribution of heat within the cell. Since a dedicated sensitivity analysis with respect to $k_{\perp}$ was not performed, its contribution to the CFD–experiment discrepancy cannot be quantified independently and is retained as a source of model uncertainty.

The two-layer subdivision does not alter the total electrochemical heat released by the cell. As stated in Equation (4), the volumetric source is defined as $\dot{q}_v = \dot{Q}/V_{\mathrm{act}}$, where V_{act} is the total volume of the active layers actually present in the model. Since the source is normalised by the same active volume over which it is applied, its integral over the active layers returns exactly $\dot{Q}$, independently of how many active and passive layers are used. The total heat released is therefore conserved for any layer subdivision, and the number of internal layers affects only the spatial distribution of the source within the cell, which is the quantity assessed in the layer-sensitivity analysis of Section 5.2.

This two-layer homogenisation approach is designed to reproduce, at a fraction of the computational cost of a fully resolved model, the macroscopic thermal anisotropy of the cell's active volume, consistently with the anisotropic heat distribution observed experimentally.

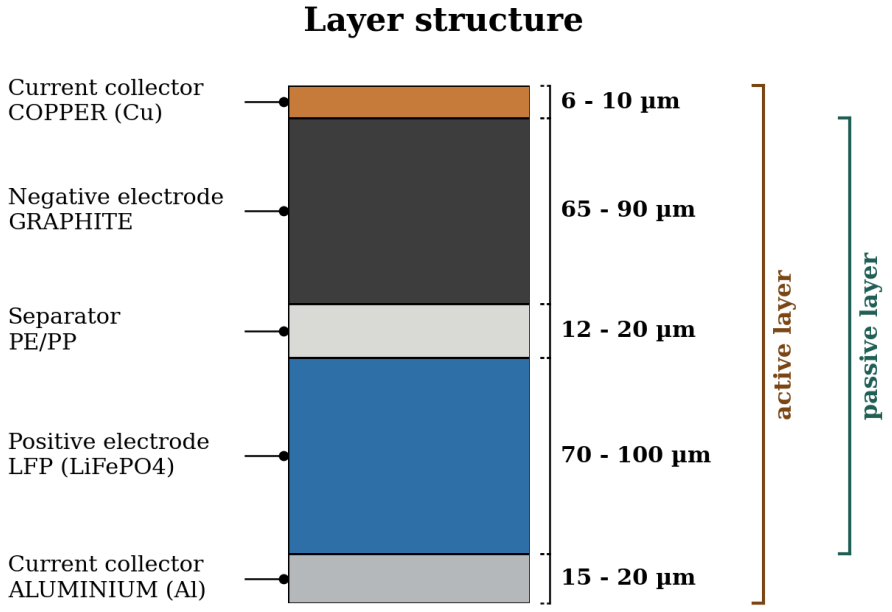

Figure 4. Schematic representation of the internal layer sequence of the prismatic LFP cell (true thickness scale), showing the grouping of sublayers into active and passive fictitious layers used in the homogenised thermal model.

3.3. CFD+CHT Coupling

The thermal behaviour of the prismatic cell was simulated by means of unsteady Reynolds-averaged Navier–Stokes simulations coupled with conjugate heat transfer. In the

present work, the term URANS is used for the transient simulations in which the Reynolds-averaged flow equations are advanced in time. The preliminary steady calculations used for initialisation are referred to as steady RANS calculations.

The flow is considered incompressible and Newtonian. The Reynolds-averaged continuity and momentum equations solved in the fluid domain are

$$\nabla \cdot \overline{\mathbf{u}} = 0, \tag{5}$$

$$\rho\left(\frac{\partial \overline{\mathbf{u}}}{\partial t} + \overline{\mathbf{u}} \cdot \nabla \overline{\mathbf{u}}\right) = -\nabla \overline{p} + \nabla \cdot \left[\mu\left(\nabla \overline{\mathbf{u}} + \nabla \overline{\mathbf{u}}^T\right) - \rho \overline{\mathbf{u}'\mathbf{u}'}\right], \tag{6}$$

where $\overline{\mathbf{u}}$ is the Reynolds-averaged velocity vector, $\overline{p}$ is the mean pressure, ρ is the fluid density, μ is the dynamic viscosity, and $-\rho\overline{\mathbf{u}'\mathbf{u}'}$ is the Reynolds-stress tensor.

The air density is treated as constant in Equation (6) and no gravity or buoyancy term is retained. A dedicated set of preliminary simulations was conducted including the Boussinesq buoyancy approximation, i.e., adding the body-force term $-\rho_\infty \boldsymbol{g}\,\beta(\overline{T} - T_\infty)$ to the right-hand side of Equation (6), with β the thermal expansion coefficient of air and T_∞ the ambient temperature, and the results were compared with the constant-density formulation. For the forced-convection cases, which represent the main operating conditions addressed in this work, the differences in the predicted wall temperature were below 0.05%, confirming that buoyancy is negligible with respect to the externally imposed airflow. For the zero-inlet-velocity cases, where buoyancy-driven motion can in principle develop, the differences remained below 0.2%, i.e., of the same order as the spatial-discretisation uncertainty quantified in Section 5.1. Within the temperature range and cycle durations investigated here, density variations therefore do not measurably affect the predicted wall temperatures, and the constant-density formulation was retained for all the simulations reported in the following in order to limit the model complexity. Since the buoyancy-augmented formulation was verified to reproduce the same wall temperatures, the zero-inlet-velocity cases are referred to as natural-convection cases throughout the manuscript.

The Reynolds-stress tensor is closed by means of the Boussinesq hypothesis for the turbulent stresses,

$$-\rho\overline{u_i'u_j'} = \mu_t\left(\frac{\partial \overline{u}_i}{\partial x_j} + \frac{\partial \overline{u}_j}{\partial x_i}\right) - \frac{2}{3}\rho k\,\delta_{ij}, \tag{7}$$

where μ_t is the turbulent viscosity and k is the turbulent kinetic energy. The SST k-ω turbulence model is adopted because of its robustness in the prediction of near-wall flows, adverse pressure gradients, and separated regions, which are expected around the sharp edges of the prismatic cell.

The energy equation is solved in the fluid domain as

$$\rho c_p\left(\frac{\partial \overline{T}}{\partial t} + \overline{\mathbf{u}} \cdot \nabla \overline{T}\right) = \nabla \cdot \left[\left(\kappa_f + \frac{\mu_t c_p}{Pr_t}\right)\nabla \overline{T}\right], \tag{8}$$

where c_p is the specific heat capacity, κ_f is the fluid thermal conductivity, and Pr_t is the turbulent Prandtl number.

In the solid regions, the transient heat-conduction equation is solved as

$$\rho_s c_{p,s}\frac{\partial T_s}{\partial t} = \nabla \cdot (\boldsymbol{\kappa}_s \nabla T_s) + \dot{q}_v, \tag{9}$$

where ρ_s, $c_{p,s}$, and $\boldsymbol{\kappa}_s$ are the density, specific heat capacity, and thermal-conductivity tensor of the solid material, respectively. The volumetric source term $\dot{q}_v$ is non-zero only in the active layers of the cell and is computed according to Equation (4).

At the fluid–solid interfaces, conjugate heat transfer is enforced by imposing the continuity of temperature and heat flux:

$$T_f = T_s, \tag{10}$$

$$-\kappa_f \nabla T_f \cdot \mathbf{n} = -\boldsymbol{\kappa}_s \nabla T_s \cdot \mathbf{n}, \tag{11}$$

where the subscripts f and s denote the fluid and solid sides of the interface, respectively, and $\mathbf{n}$ is the interface normal vector.

3.4. Simulation Setup

The computational domain was defined using the battery height H as the reference length. The cell was positioned sufficiently far from the inlet to allow the incoming flow to develop before interacting with the battery, while the downstream extension was selected to avoid outlet interference with the wake. The domain extends $25H$ in the streamwise direction and $6H \times 6H$ in the two cross-stream directions, with the leading edge of the cell located $7H$ (1.3 m) downstream of the inlet and $18H$ upstream of the outlet. Figure 5 shows the computational domain and the main boundary conditions adopted in the simulations.

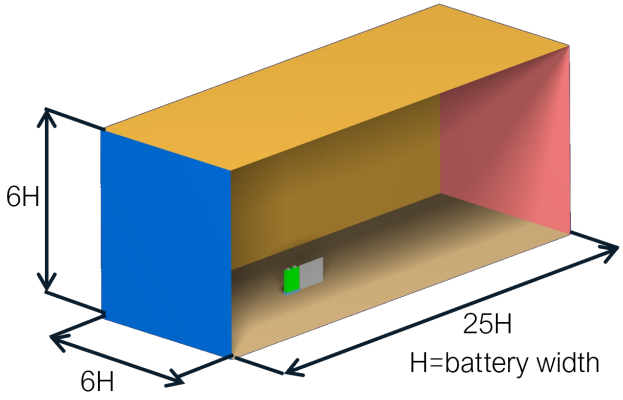

Figure 5. Computational domain and boundary conditions adopted for the CFD+CHT simulations of the prismatic cell.

For the forced-convection cases, a uniform velocity is imposed at the inlet (blue boundary in Figure 5),

$$\overline{\mathbf{u}}_{\text{in}} = (U_{\text{in}}, 0, 0), \tag{12}$$

with $U_{\text{in}} = 10\ \text{m s}^{-1}$ or $20\ \text{m s}^{-1}$. The inlet turbulence is specified through the turbulence intensity and the turbulent length scale. The intensity is set to 0.9%, equal to the value measured in the empty test section of the wind tunnel (see Section 4), and the length scale to $\ell = 18$ mm, i.e., half the reference dimension of the cell ($\ell/D^* = 0.5$), so that the energy-containing eddies of the incoming stream are smaller than the body they invest. For natural convection, no imposed incoming flow is applied. The inlet air temperature is set equal to the experimentally measured ambient temperature. The initial temperature of the solid region (battery and support) is likewise set equal to the ambient value, consistently with the experimental conditions at the start of each test. A pressure-outlet condition is imposed at the outlet (red surface in Figure 5), no-slip conditions are applied on the battery, support, flat-plate, and ground surfaces (green and grey surfaces in Figure 5), and a slip wall condition (zero tangential stress, zero normal velocity) is imposed on the lateral and top boundaries of the domain. The no-slip condition on the ground boundary reproduces the wind-tunnel floor, which generates a turbulent boundary layer upstream of the cell;

the height of the 3D-printed support was dimensioned accordingly, so as to position the battery at the appropriate distance from the floor, consistently with the experimental setup.

The fluid domain was discretised with a hexa-dominant unstructured mesh, whose cell size is progressively refined towards the cell and its near wake and coarsened towards the far-field boundaries, while near-wall prism layers were introduced on the battery and support surfaces in order to resolve the boundary-layer region and improve the prediction of the convective heat transfer. The SST k-ω model was used with a low-Reynolds near-wall treatment, i.e., the viscous sublayer is resolved rather than bridged by a wall function. Accordingly, the prism-layer mesh on the battery and support surfaces was designed so that the wall-normal coordinate of the first cell centroid satisfies $y^+ \approx 1$ at the highest free-stream velocity, $U_{\text{in}} = 20\ \text{m s}^{-1}$, which is the most demanding condition. The stack consists of 18 prism layers with a first-layer thickness of 0.03 mm and a geometric growth rate of 1.2, followed by two additional transition layers used to match the last prism to the size of the adjacent volume cells, for a total prism-layer thickness of approximately 3.8 mm. This thickness is of the same order as the near-wall shear-layer thickness developing along the lateral faces at the highest velocity, so that the region controlling the convective heat flux is contained within the structured near-wall mesh. The solid regions were discretised consistently with the internal layered structure of the cell, ensuring that active and passive layers were represented as separate volumetric regions. The flow and energy equations were solved with a finite-volume method, using second-order upwind schemes for the convective terms of the momentum, energy and turbulence equations, and a second-order implicit scheme for time advancement. A pressure-based coupled algorithm was adopted, in which the momentum and pressure-based continuity equations are solved simultaneously rather than sequentially; this choice is significant for the present transient strategy, because the coupled formulation remains robust at the large convective Courant numbers associated with the time step used in the thermal phase, which a segregated pressure-correction scheme would not tolerate as efficiently. Fifteen inner iterations were performed within each time step, which were verified to be sufficient for the scaled residuals of the continuity, momentum, turbulence and energy equations to meet the convergence criteria before advancing in time. Convergence was further monitored through the relative change of the battery surface temperature between consecutive time steps, which remained below 1%. More details on the grids considered in the present study and the assessment of grid independence are provided in Section 5.1.

Transient Simulation Strategy

A dedicated transient strategy was adopted to separate the initialisation of the external flow field from the thermal evolution of the battery. The procedure consists of three steps.

First, a steady RANS simulation without internal heat generation is performed. Convergence is assessed through the monitoring of the flow residuals, which are required to reach a sufficiently low level before advancing to the next phase. Second, the simulation is advanced in unsteady RANS mode without heat generation using a second-order implicit time discretisation and a time step of $\Delta t = 10^{-4}$ s, in order to develop the unsteady velocity field around the battery and the downstream flat plate. The transition to the third phase is triggered when the flow field in the vicinity of the cell has reached a stationary condition, as confirmed by the stabilisation of the instantaneous velocity and pressure fields and by the absence of significant low-frequency oscillations in the monitored flow quantities. Third, the coupled CFD+CHT transient is started: the volumetric heat source is activated inside the active layers, the time step is increased to $\Delta t = 10$ s and kept constant for the entire duration of the electrical cycle, while the second-order implicit time discretisation is retained for consistency with the previous phase.

The value $\Delta t = 10$ s adopted in the third phase is much larger than the convective time scale of the external flow, and it is therefore worth clarifying why it does not compromise the solution. The reason is twofold. First, the time integration is performed with a second-order implicit scheme, which is unconditionally stable: the large convective Courant number associated with $\Delta t = 10$ s at $U_{\text{in}} = 10$–20 m s^{-1} does not violate any stability limit. Second, and more importantly, the accuracy requirement in the third phase is set by the thermal problem and not by the aerodynamic one. The two phenomena are separated by several orders of magnitude in time scale: the aerodynamic field develops over $\mathcal{O}(H/U_{\text{in}}) \sim 10^{-2}$ s, whereas the wall temperature evolves over the duration of the electrical cycle, $\mathcal{O}(10^3)$ s. The velocity field and the resulting mean convective heat-transfer coefficient are brought to a statistically stationary state in the second phase with $\Delta t = 10^{-4}$ s, and they no longer evolve on the slow thermal time scale. In the third phase, Δt must therefore resolve only the slow thermal transient, not the fast turbulent fluctuations, whose instantaneous effect on the cycle-scale wall temperature averages out. The adequacy of $\Delta t = 10$ s was verified through a dedicated time-step sensitivity test, in which the whole thermal transient of the 2C charge case at $v = 20$ m s^{-1}, i.e., the most demanding condition of the test matrix, was repeated with $\Delta t = 1$, 5 and 10 s. The predicted wall temperatures at the probe locations differed by less than 1%, i.e., by a negligible amount compared with the numerical–experimental deviations discussed in Section 6. Time steps larger than 10 s were not considered, so as to keep the convective Courant number within a range for which the second-order implicit scheme retains its formal accuracy. The adequacy of the adopted time step during the thermal transient was further verified by checking that the relative temperature increase at the battery surface between consecutive steps remained below 1%, confirming that the selected Δt was sufficient to capture the relevant thermal gradients. At each time step, the heat-generation routine reads the local temperature of each active control volume and updates $\dot{q}_v$ according to the interpolated electrochemical–thermal model. The simulated physical time is equal to 60 min for 1C cycles and 30 min for 2C cycles.

This strategy allows the flow field to be stabilised before the heat source is introduced, while the subsequent battery heating is computed with a time step appropriate for the thermal dynamics. As a result, the method retains the coupling between surface heat transfer and internal heat generation without requiring the full operating cycle to be resolved at the smallest aerodynamic time scale.

4. Experimental Validation

The experimental campaign was carried out in the wind tunnel of the Department of Civil and Industrial Engineering of the University of Pisa. The objective of the tests was to provide a reliable dataset for the validation of the CFD+CHT model by measuring the wall-temperature distribution of the cell under controlled electrical and aerodynamic operating conditions.

Probe positioning is referred to the instrumented-battery layout shown in Figure 6. The same probe locations are used later for the extraction of CFD temperatures, so that numerical and experimental data are compared point by point on the external battery surface.

The facility is a subsonic closed-jet wind tunnel with an open test section. The test section has a circular cross-section with a diameter of 1.10 m and a length of 1.42 m, and it can operate in a velocity range between 5 and 35 m s^{-1}. The free-stream turbulence intensity is approximately 0.9%. The reference frame is defined with the x-axis aligned with the incoming flow, the z-axis directed vertically upward, and the y-axis completing the right-handed system.

The battery was mounted on the mid-plane of the test section by means of a dedicated 3D-printed support. The same downstream flat plate used in the numerical model was also

included in the experimental setup, in order to ensure consistency between the CFD and wind-tunnel configurations. The electrical connections were arranged so as to minimise their influence on the external flow field.

The thermal instrumentation consisted of one Pt100 thermoresistance used to measure the ambient air temperature and 28 type-K thermocouples mounted on the external surface of the battery. The thermocouples were arranged on four horizontal planes along the cell height, as shown in Figure 6. Since preliminary tests showed a substantially symmetric temperature distribution with respect to the vertical mid-plane aligned with the incoming flow, thermocouples were installed on only one of the two lateral faces.

The thermocouples were attached to the external surface of the cell by means of aluminium adhesive tape, with the junction pressed flat against the wall and fully covered by the tape, so as to minimise both the thermal contact resistance and the exposure of the junction to the external airflow. The leads were routed along the local isotherms for a short distance before leaving the surface, in order to limit the conduction error along the wires. The same attachment procedure, the same tape and the same patch size were used at all 28 locations, in order to minimise systematic differences among the probes; however, residual local attachment and airflow effects cannot be completely excluded. The signals were acquired through a National Instruments NI 9219 module. The module has a 24-bit ADC and a NIST-traceable factory calibration, applies per-channel cold-junction compensation, and converts the thermoelectric voltage to temperature using the ITS-90 reference functions [37,38]. No further in-house calibration of the individual thermocouples was performed; the calibration relied on the traceable calibration of the acquisition chain, complemented by the in situ differential check described below.

The nominal type-K tolerance of ± 1.5 °C (IEC 60584-1, Class 1) [38] is a worst-case sensor-lot value and is not representative of the uncertainty of the present measurement chain. The relevant figure is the accuracy of the calibrated acquisition chain, documented in the module specifications [39]: on the thermocouple (± 125 mV) range the offset error is ± 120 ppm of range (about ± 0.37 °C) and the gain error is $\pm 0.1\%$ of reading, while the cold-junction-compensation accuracy is ± 1 °C. Combining these contributions, the absolute temperature accuracy is approximately ± 1 °C, dominated by the cold-junction compensation.

Since spatial temperature differences over the cell surface constitute an important component of the validation, the channel-to-channel consistency of the acquisition system was also assessed. This quantity should be distinguished from the complete uncertainty associated with spatial temperature differences during operation. The assessment was performed in situ from the isothermal rest condition preceding each test: with no applied current and the wind tunnel switched off, all 28 thermocouples equilibrate to the same ambient temperature and must therefore read the same value, so that their spread is a direct measure of the channel-to-channel consistency. Applying a per-channel offset correction derived from this condition removes the common cold-junction bias together with the individual channel offsets, leaving a residual scatter at the level of the module input noise and gain matching, i.e., within ± 0.1 °C. This residual scatter should therefore be interpreted as a measure of the channel-to-channel consistency under the initial isothermal condition, rather than as the complete uncertainty of spatial temperature differences during the experiment. Additional contributions associated with thermocouple characteristics, surface attachment, local airflow around the junction and leads, and temperature-dependent effects were not independently quantified in the present campaign. Repeating the isothermal soak at the beginning of every test also provides a run-to-run repeatability check. Each operating condition of the test matrix was repeated three times, and the end-of-cycle temperatures were reproducible to within ± 0.2 °C; the values reported in the following are the averages over the three repetitions.

The wind-tunnel air temperature is not actively controlled. All tests were therefore performed within a narrow ambient window of 22.5–24.5 °C, in the same season and at the same time of day, discarding the warmer days, and the measured temperatures were normalised to a common reference ambient of 23.5 °C. This normalisation is justified because, under convective cooling, the steady temperature rise above ambient $\Delta T = \dot{Q}/(hA)$ is set by the heat generation and by the convective conductance and is essentially independent of the absolute ambient level (Newton's law of cooling); over a window of only ±1 °C, the air properties and the convective heat-transfer coefficient are unchanged, so that the cell temperature field shifts rigidly with the ambient temperature. This near-linear, nearly one-to-one shift of the cell temperature with the ambient level is consistent with experimental studies that characterise the temperature field of prismatic cells over ambient ranges of several tens of degrees, far wider than the 2 °C window adopted here [40,41].

Charge and discharge cycles were imposed using a battery cycler composed of a 60 V–250 A Ametek SPS60x250-K02D (AMETEK Programmable Power, San Diego, CA, USA) charger and a 60 V–500 A Zentro-Elektrik EL6000 discharger (Zentro Elektronik, Bad Wildbad, Germany). Voltage and current were measured using a National Instruments DAQ 9219 (National Instruments Corporation, Austin, TX, USA) with an acquisition rate of 100 ms. The complete acquisition system was synchronised through LabVIEW, version 16.0 (2016), allowing the electrical quantities, wind-tunnel conditions, ambient temperature, and thermocouple measurements to be recorded consistently during the whole test.

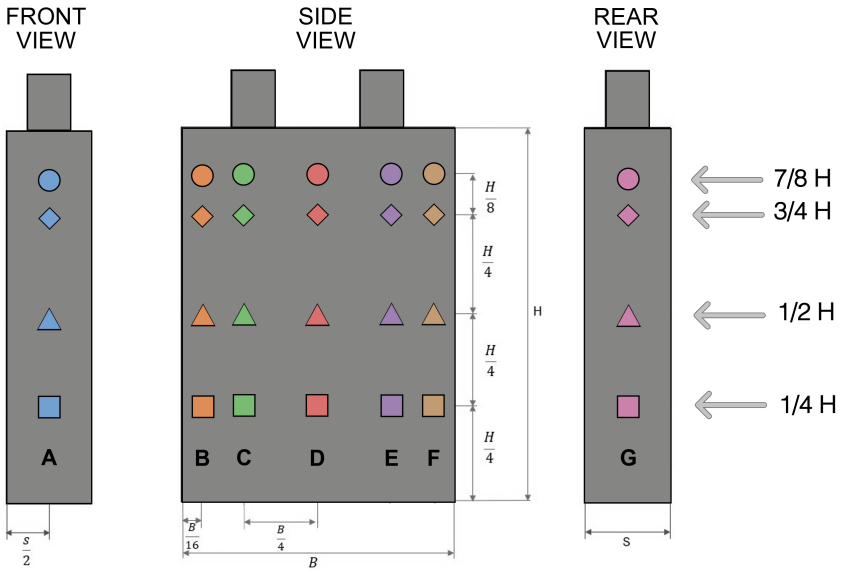

Figure 6. Thermocouple layout adopted on the external surfaces of the prismatic $LiFePO_4$ cell. This layout defines the probe positions used for the experimental acquisition and for the extraction of the corresponding CFD temperatures.

The experimental setup was therefore designed to reproduce, as closely as possible, the physical conditions imposed in the CFD+CHT model. The resulting dataset is used in Section 6 to validate the numerical temperature field on the external surface of the battery.

5. Grid and Layer Sensitivity

Before analysing the operating conditions in the test matrix, two numerical sensitivity checks were performed. The first one concerned the computational grid used in the fluid and solid domains, while the second one concerned the number of equivalent internal layers used to represent the battery stack. The objective was to identify a configuration that

was sufficiently resolved for the present heat-transfer problem while remaining compatible with future extensions to module-level calculations.

5.1. Grid Sensitivity

The grid sensitivity was assessed by comparing the wall-temperature field and the main wake features for progressively refined meshes. Particular attention was paid to the near-wall prism layers on the battery surfaces, because the local thermal boundary layer controls the convective heat flux exchanged between the cell and the external flow. The selected grid preserves the location of the main recirculation region behind the battery and provides stable values of the surface temperature at the thermocouple locations. This check is especially relevant for the forced-convection cases, where the thermal gradients are driven by the interaction between the separated wake, the downstream flat plate, and the local convective heat-transfer coefficient.

Several mesh refinement levels were considered in order to define the final computational grid. The sensitivity analysis was carried out by comparing the maximum and minimum temperatures predicted in the battery measurement regions at the end of the charging cycle. These quantities were selected because they provide a direct indication of both the peak thermal response and the spatial temperature range expected at the locations used for numerical–experimental comparison. The results of the mesh sensitivity analysis are summarised in Table 3.

Table 3. Mesh sensitivity analysis based on the maximum, minimum and mean temperatures evaluated in the battery measurement regions.

Mesh Level	Cells ($\times 10^6$)	T_{max} (°C)	T_{min} (°C)	T_{avg} (°C)
Coarse mesh	0.3	33.67	26.43	30.22
Medium mesh	0.7	32.01	25.78	29.31
Fine mesh	1.5	31.05	25.97	28.07
Extra-fine mesh	3.0	30.98	25.95	28.02

The temperature extrema show that the solution becomes nearly insensitive to further refinement when moving from the fine to the extra-fine mesh.

Refining the mesh from the selected fine grid (1.5×10^6 cells) to the extra-fine grid (3.0×10^6 cells) modifies the predicted extrema by less than 0.25% (T_{max} from 31.05 to 30.98 °C, T_{min} from 25.97 to 25.95 °C) and the mean wall temperature by 0.18% (28.07 to 28.02 °C). The selection of the fine grid was based on this trade-off, namely the almost negligible differences in the predicted temperature extrema compared with the extra-fine grid, together with its significantly lower computational cost. We also remark that the sensitivity study was carried out for the 2C charge case at $v = 10\ \mathrm{m\,s^{-1}}$, i.e., the condition with the strongest variation of the temperature along the cell surface. Under forced convection, the local extrema are governed by the near-wall prism-layer resolution on the fluid side, which resolves the spatial variation of the convective heat-transfer coefficient, rather than by the through-thickness discretisation of the solid, which is addressed separately in Section 5.2.

5.2. Layers Sensitivity

Before analysing the thermal behaviour of the battery under the different operating conditions, a sensitivity analysis was performed on the number of internal layers used in the CAD representation of the cell. The test was carried out for the 1C cycle under natural-convection conditions, which was selected as a reference case to evaluate the influence of the internal layering on the predicted thermal response. This analysis was aimed at selecting a geometrical configuration able to preserve the thermal response of the real layered structure

while reducing the number of volume elements and, consequently, the computational cost of the CFD+CHT simulations. Figure 7 reports the mean temperature of the active volume as a function of the number of internal layers, together with the corresponding number of volume elements.

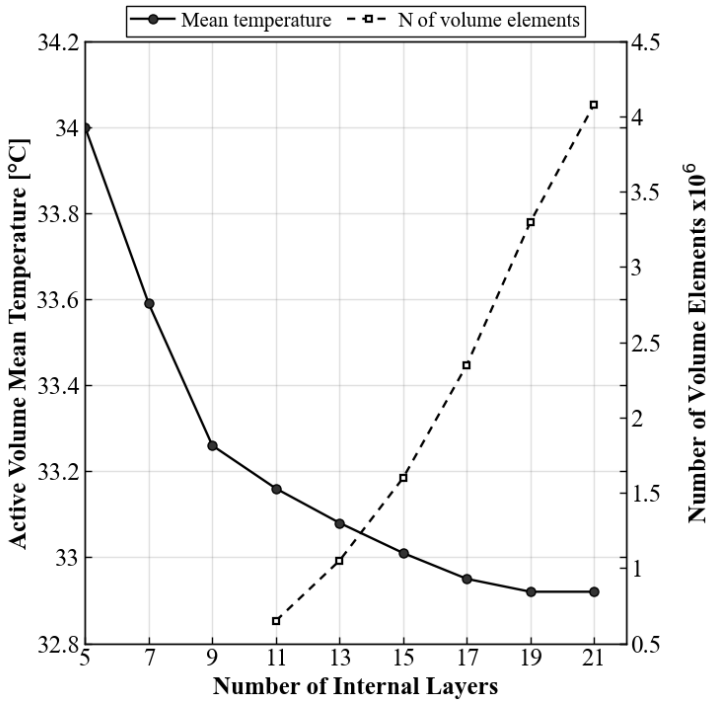

Figure 7. Sensitivity analysis on the number of internal layers used in the CAD representation of the cell for the 1C charge cycle under natural-convection conditions. The mean temperature of the active volume at end of cycle is reported together with the corresponding number of volume elements.

The results show that the mean temperature decreases progressively as the number of internal layers increases, approaching an asymptotic value for the most refined configurations. This behaviour indicates that a more detailed representation of the internal layered structure improves the description of heat conduction within the cell, but also leads to a significant increase in the number of volume elements. The configuration with 15 internal layers was therefore selected as a compromise between accuracy and computational efficiency. It provides an acceptable deviation from the most refined cases while substantially reducing the size of the computational domain and the associated simulation time.

The difference between the selected configuration and the most refined one can be quantified explicitly: the mean temperature of the active volume at end of cycle is 33.01 °C for the 15-layer model and 32.93 °C for the 21-layer model, i.e., a difference of 0.08 °C, or 0.24%, obtained with 2.7 times fewer volume elements (1.5 against 4.1 million). This residual difference is of the same order as the spatial-discretisation error quantified in Section 5.1 (0.18–0.25% between the fine and the extra-fine grid), so that neither of the two discretisation parameters dominates the numerical uncertainty of the present setup. It is also useful to distinguish the roles of the two discretisation parameters examined in this section. The internal layer count controls the anisotropic heat conduction through the thickness of the cell, i.e., the internal temperature distribution, whereas the local temperature extrema on the external surface under forced convection are controlled by the near-wall grid resolution on the fluid side discussed in Section 5.1. The selected combination of fine mesh and 15 internal layers therefore represents the best compromise between local temperature accuracy and computational cost for both mechanisms.

To complement the analysis based on the temperature extrema and on the mean active-volume temperature, Figure 8 compares the time evolution of the wall temperature at three representative thermocouple locations for the different mesh and layer resolutions, using as test case 2C charge cycle at $v = 10\ \mathrm{m\,s^{-1}}$. The curves are practically indistinguishable, confirming that the selected configuration reproduces not only the temperature extrema and the mean level, but also the local temperature histories at the probe positions used for the numerical–experimental comparison.

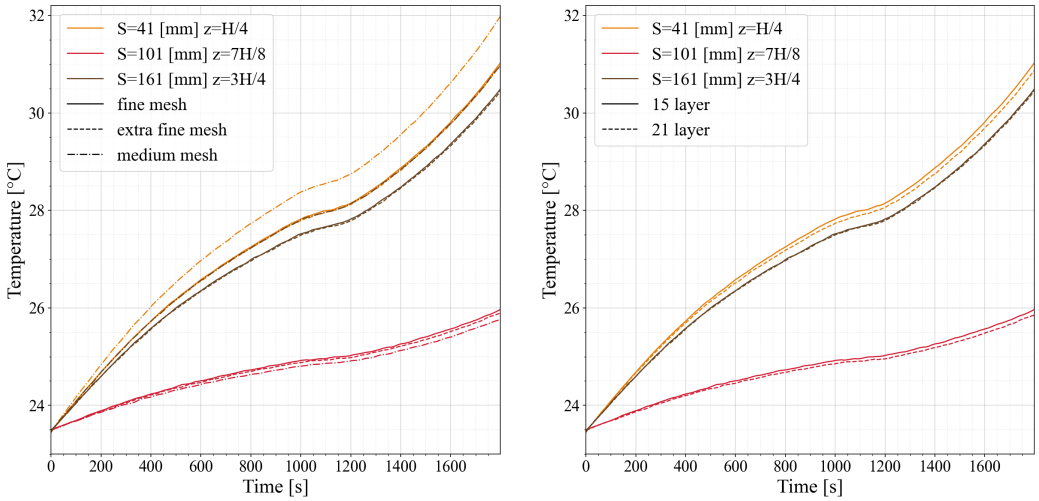

Figure 8. Time evolution of the wall temperature at three representative thermocouple locations for the 2C charge cycle at $v = 10\ \mathrm{m\,s^{-1}}$. (**Left**): Fine (solid) and extra-fine (dashed) mesh; (**Right**): 15-layer (solid) and 21-layer (dashed) internal discretisation.

6. Results

In this section, the CFD+CHT results are first interpreted in terms of wall-temperature distribution, flow-field effect, and thermal uniformity. The numerical predictions are then compared with the experimental measurements acquired during the wind-tunnel campaign. The comparison is carried out at the thermocouple positions shown in Figure 6, which define the common probe locations for the experimental acquisition and for the numerical post-processing.

Before discussing the individual operating conditions, it is important to note that both the numerical and experimental results show a substantially symmetric wall-temperature distribution with respect to the xz plane, i.e., the vertical plane aligned with the main flow direction. As a consequence, the thermal behaviour on the two lateral faces can be considered equivalent, and the comparison between CFD and experiments can be discussed on the basis of the selected measurement planes and surface probes.

The temperature distributions are compared at the same normalised time instants of the cycle. In the following, the normalised time τ is defined as

$$\tau = \frac{t_{\mathrm{phys}}}{t_{\mathrm{cycle}}}, \tag{13}$$

where t_{phys} is the physical time and t_{cycle} is the total duration of the considered charge or discharge cycle. In this way, the selected instants are independent of the specific C-rate and represent the same relative stage of the operating cycle.

For both 1C and 2C cycles, and for both charge and discharge conditions, the battery heating is approximately monotonic over time. The thermal evolution follows the response surface obtained from the interpolation of the electrochemical–thermal model implemented

in the CFD code. This confirms that the coupling strategy adopted between the volumetric heat-generation law and the conjugate heat-transfer model is able to reproduce consistently the progressive increase in wall temperature throughout the cycle.

Since the methodology is transient, the validation is not restricted to the end-of-cycle condition nor to a single probe. This behaviour is illustrated in Figure 9, where the time evolution of the wall temperature is compared with the corresponding CFD prediction at three representative thermocouple locations and for three different operating conditions: the 2C charge cycle at $v = 10\ \mathrm{m\,s^{-1}}$ (Figure 9a), the 2C discharge cycle at the same air velocity (Figure 9b) and the 2C charge cycle at $v = 20\ \mathrm{m\,s^{-1}}$ (Figure 9c). The transient comparison therefore covers both cycle directions and two different convective regimes. The probes are distributed both along the cell height and along the curvilinear coordinate S: $S = 41$ mm at $z = H/4$, $S = 161$ mm at $z = 3H/4$, and $S = 101$ mm at $z = 7H/8$. Here, S is the curvilinear coordinate, expressed in millimetres, measured along the external surface from the outer edge of the front face, around the lateral face, to the outer edge of the rear face. The three probes therefore sample both the front and the rear portions of the lateral surface and three different heights.

In all three cases, the overall temperature rise is approximately monotonic at all three locations, and the CFD prediction follows the experimental transient throughout the cycle, reproducing not only the temperature level but also the vertical stratification: the probe closest to the top of the cell remains consistently colder than the two lower ones, and the model captures the separation between the two groups of curves from the very beginning of the transient. A transient reduction in the rate of temperature increase, associated with the drop in volumetric heat-generation rate visible in Figure 3b, is reproduced by the CFD model and is also identifiable in the experimental measurements. The agreement observed at the end of the cycle is therefore representative of the whole thermal transient rather than of a single time instant.

The discharge cycle of Figure 9b and the higher-velocity charge cycle of Figure 9c show the same behaviour: the ordering of the three probes, the overall heating rate and the change of slope in the central part of the cycle are reproduced in both cases, showing that a comparable quality of the transient prediction is obtained for the investigated cycle directions and convective conditions. In all three conditions, the largest deviation is found at the lowest probe ($S = 41$ mm, $z = H/4$), where the model underestimates the measured temperature over the final part of the cycle, consistently with the maximum local error discussed later in this section.

Thermal uniformity was evaluated using three complementary scalar indices computed at the $N = 28$ thermocouple probe locations at the end of each cycle. The temperature spread and the standard deviation are defined as

$$\Delta T = T_{\max} - T_{\min}, \tag{14}$$

$$\sigma_T = \sqrt{\frac{1}{N}\sum_{i=1}^{N}\left(T_i - T_{\mathrm{avg}}\right)^2}, \tag{15}$$

where T_i is the temperature at the i-th probe and T_{avg} is the mean over the N probes. A third index is the uniformity index γ, following the scalar formulation adopted in CFD analysis of flow and temperature distributions [42],

$$\gamma = 1 - \frac{1}{N\,T_{\mathrm{avg}}}\sum_{i=1}^{N}\left|T_i - T_{\mathrm{avg}}\right|, \tag{16}$$

where $\gamma = 1$ corresponds to a perfectly uniform field and $\gamma \to 0$ to maximum non-uniformity. All three indices are evaluated with temperatures expressed in degrees Celsius. This choice is essential for γ: if temperatures are expressed in Kelvin, the mean denominator $T_{\mathrm{avg}} \approx 300$ K greatly exceeds the typical battery temperature spreads ($\mathcal{O}$(1–10 °C)), forcing $\gamma \to 1$ for every case and suppressing its discriminating power. It must be acknowledged that, for this same reason, γ as defined in Equation (16) is not invariant under a change of temperature scale: its value depends on the arbitrary zero of the scale through T_{avg}. Degrees Celsius are adopted here because they are the de facto standard for thermal-uniformity metrics in battery thermal management, where both the reported temperatures and the design constraint $\Delta T < 5$ °C are conventionally expressed in °C. For completeness, and in order to provide a metric that is independent of the temperature reference, a normalised uniformity index is also defined as

$$\gamma^{*} = 1 - \frac{1}{N\,\Delta T_{\mathrm{ref}}} \sum_{i=1}^{N} \left| T_i - T_{\mathrm{avg}} \right|, \tag{17}$$

where ΔT_{ref} is a fixed, physically motivated reference temperature difference. In the present work, $\Delta T_{\mathrm{ref}} = 5$ °C is adopted, corresponding to the commonly used upper limit for acceptable temperature non-uniformity in battery thermal-management applications. Since ΔT_{ref} is defined independently of the present dataset and represents a temperature difference rather than an absolute temperature, γ^{*} is both dataset-independent and invariant under a change of temperature scale. The values of γ^{*} are reported alongside γ in Tables 4 and 5.

Table 4. Thermal uniformity indices at end of cycle for the charge cases, computed on the $N = 28$ probe locations. All temperatures in °C. γ^{*} is the reference-independent index of Equation (17), evaluated with $\Delta T_{\mathrm{ref}} = 5$ °C.

C-Rate	Cooling Condition	Source	$T_{\max}$	T_{avg}	ΔT	σ_T	γ	γ^{*}
1C	Natural convection	CFD	34.23	32.12	3.25	0.961	0.9755	0.843
		EXP	33.04	32.38	1.53	0.394	0.9904	0.938
	$v = 10\ \mathrm{m\,s^{-1}}$	CFD	29.06	27.55	2.61	0.766	0.9763	0.869
		EXP	28.92	28.14	1.89	0.545	0.9836	0.908
	$v = 20\ \mathrm{m\,s^{-1}}$	CFD	27.28	25.77	2.82	0.755	0.9758	0.875
		EXP	27.22	25.44	3.45	1.053	0.9638	0.816
2C	Natural convection	CFD	41.78	39.36	4.17	1.257	0.9735	0.791
		EXP	41.38	39.54	3.29	0.935	0.9796	0.839
	$v = 10\ \mathrm{m\,s^{-1}}$	CFD	33.13	30.25	5.16	1.437	0.9616	0.768
		EXP	34.27	30.69	6.42	1.777	0.9541	0.718
	$v = 20\ \mathrm{m\,s^{-1}}$	CFD	31.08	28.07	5.24	1.462	0.9579	0.764
		EXP	32.14	28.59	6.59	1.896	0.9432	0.675

Table 5. Thermal uniformity indices at end of cycle for the discharge cases, computed on the $N = 28$ probe locations. All temperatures in °C. γ^{*} is the reference-independent index of Equation (17), evaluated with $\Delta T_{\mathrm{ref}} = 5$ °C.

C-Rate	Cooling Condition	Source	$T_{\max}$	T_{avg}	ΔT	σ_T	γ	γ^{*}
1C	Natural convection	CFD	33.71	31.63	3.22	0.950	0.9754	0.844
		EXP	32.54	31.88	1.53	0.394	0.9902	0.938
	$v = 10\ \mathrm{m\,s^{-1}}$	CFD	28.26	26.77	2.59	0.756	0.9760	0.872
		EXP	28.12	27.34	1.89	0.545	0.9831	0.908
	$v = 20\ \mathrm{m\,s^{-1}}$	CFD	26.88	25.36	2.83	0.758	0.9753	0.875
		EXP	26.82	25.04	3.45	1.053	0.9632	0.816
2C	Natural convection	CFD	41.28	38.86	4.16	1.251	0.9733	0.792
		EXP	40.88	39.04	3.29	0.935	0.9794	0.839
	$v = 10\ \mathrm{m\,s^{-1}}$	CFD	32.26	29.36	5.18	1.440	0.9603	0.767
		EXP	33.37	29.79	6.42	1.777	0.9527	0.718
	$v = 20\ \mathrm{m\,s^{-1}}$	CFD	30.79	27.77	5.25	1.465	0.9573	0.763
		EXP	31.84	28.29	6.59	1.896	0.9426	0.675

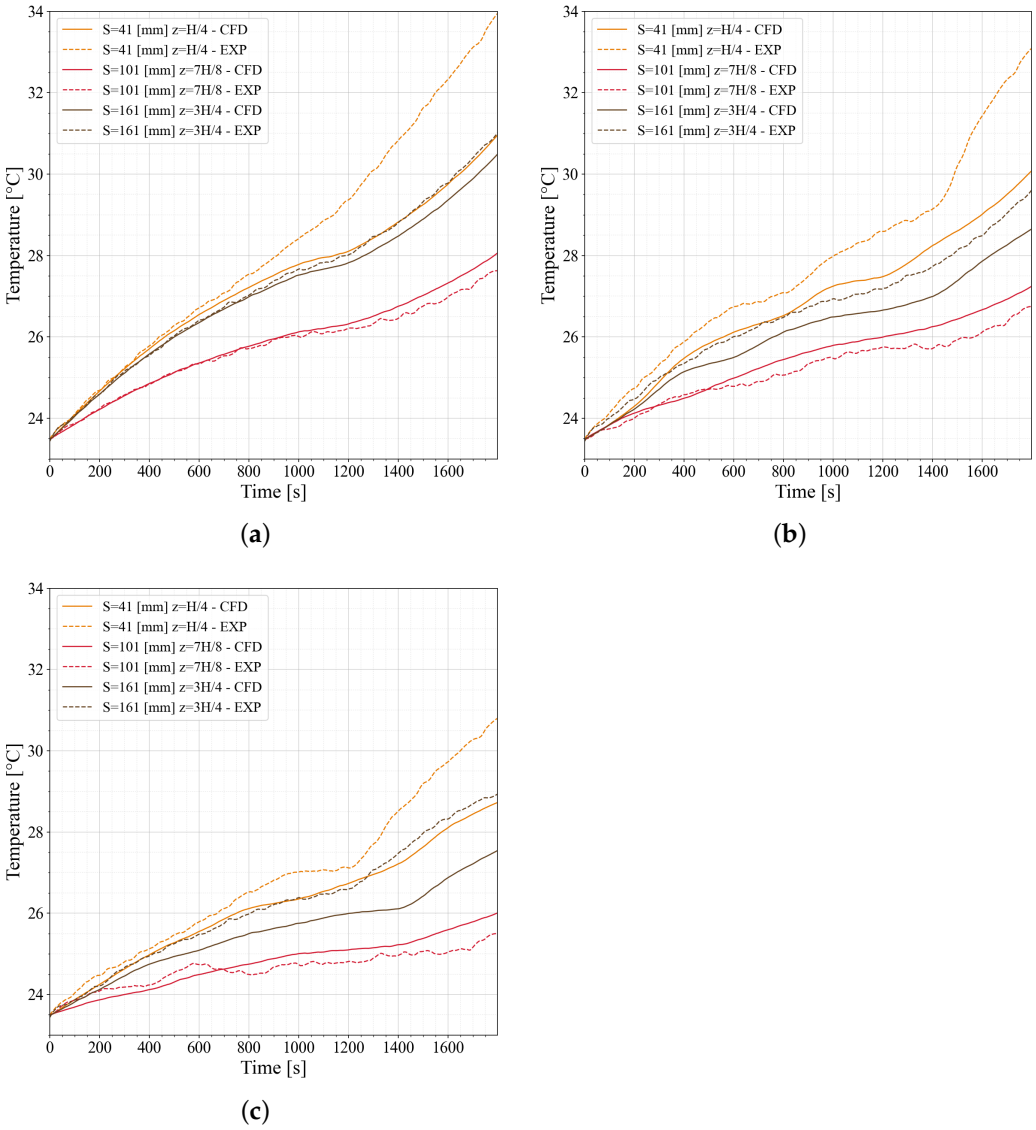

Figure 9. Time evolution of the wall temperature at three representative thermocouple locations: $S = 41$ mm, $z = H/4$; $S = 161$ mm, $z = 3H/4$; $S = 101$ mm, $z = 7H/8$. CFD predictions (solid) are compared with the experimental measurements (dash). (**a**) 2C charge cycle at $v = 10\ \mathrm{m\,s^{-1}}$; (**b**) 2C discharge cycle at $v = 10\ \mathrm{m\,s^{-1}}$; (**c**) 2C charge cycle at $v = 20\ \mathrm{m\,s^{-1}}$.

Comparing the two indices is instructive. For the experimental data the two rankings coincide, and the conclusion that the natural-convection cases are the most uniform and the 2C forced-convection case at 20 $\mathrm{m\,s^{-1}}$ the least uniform is confirmed by both indices. For the CFD data at 1C, however, the two indices disagree: γ ranks the natural-convection case ($\gamma = 0.9755$) as marginally more uniform than the forced-convection case at 20 $\mathrm{m\,s^{-1}}$ ($\gamma = 0.9758$) is, whereas γ^* reverses the order (0.843 against 0.875). The origin of the discrepancy is precisely the reference dependence of γ: the natural-convection cases have a much higher mean level ($T_{\mathrm{avg}} = 32.12$ against 25.77 °C), and normalising the deviations by T_{avg} rewards the hotter case. The reference-independent index γ^* is therefore preferable when cases at appreciably different mean temperature levels are compared, while γ is retained here for continuity with the literature [42]. The differences affect only cases whose uniformity is nearly identical, and none of the conclusions drawn in the following depends on the choice of index.

Together, the three indices serve complementary roles. The index γ provides a single scalar for ranking all cases by uniformity. The range ΔT allows direct comparison

against the common battery thermal management constraint of $\Delta T < 5\,^{\circ}\mathrm{C}$. The standard deviation σ_T characterises the spatial distribution of deviations and, combined with the wall-temperature maps, helps distinguish between a diffuse in-plane gradient—driven by the non-uniform convective cooling of the exposed surfaces—and a more localised hot spot, which would manifest as a high ΔT with a comparatively lower σ_T.

6.1. CFD+CHT Results

6.1.1. Charge Cycles

The wall-temperature evolution during the 1C and 2C charge cycles is reported in Figures 10 and 11, respectively. Under natural convection, the battery heats up in a substantially homogeneous way. The absence of an imposed external flow limits the development of preferential cooling regions on the external surfaces, and the temperature field remains nearly uniform over the entire battery wall. The thermal behaviour is therefore mainly governed by internal heat conduction and by the weak heat exchange with the surrounding air.

When forced convection is introduced, the wall-temperature field becomes progressively non-uniform. For both 1C and 2C cycles, vertical and in-plane gradients appear due to the interaction between the external flow and the battery surfaces. These gradients become more pronounced as the airflow velocity is increased from 10 m s^{-1} to 20 m s^{-1}. In particular, the wall temperature in the central region of the lateral surface is lower than in the areas closer to the battery edges, as well as lower than on the front and rear faces. The 2C charge cycle shows larger temperature differences because of the higher heat-generation rate.

Figure 10 shows the 1C charge case. The natural-convection panel is dominated by conduction inside the cell and therefore exhibits only weak spatial gradients. At 10 m s^{-1}, the external flow starts to impose a clear preferential cooling pattern on the exposed surfaces, with lower temperatures in the regions most directly affected by the incoming stream. At 20 m s^{-1}, the same pattern is amplified: the mean temperature decreases, but the temperature spread increases because the forced convective removal is not spatially uniform.

Figure 11 reports the same cooling sequence for the 2C charge case. Since the electrical load is higher, the internal heat-generation rate increases and the wall-temperature level rises more rapidly. The natural-convection condition remains comparatively uniform, while the two forced-convection cases show stronger gradients than in the 1C cycle. This behaviour indicates that increasing the airflow velocity improves heat removal but also makes the thermal field more sensitive to local flow separation and wake development.

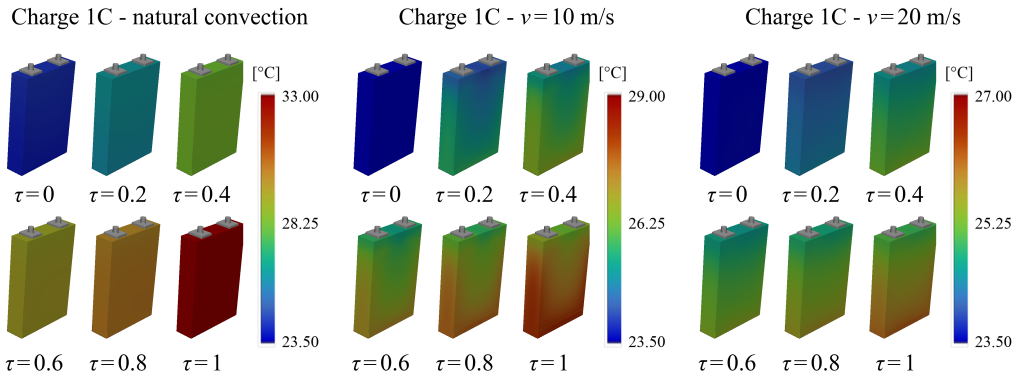

Figure 10. Wall-temperature distribution during the 1C charge cycle. Left to right: natural convection, $v = 10$ m s^{-1}, and $v = 20$ m s^{-1}.

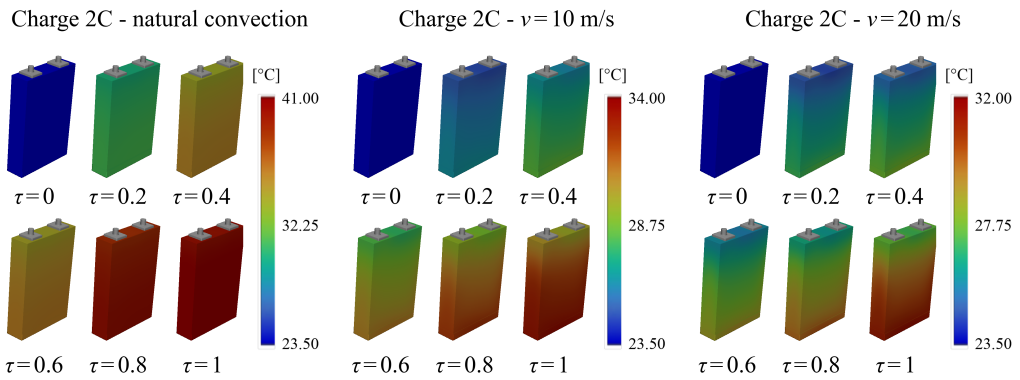

Figure 11. Wall-temperature distribution during the 2C charge cycle. Left to right: natural convection, $v = 10\ \mathrm{m\,s^{-1}}$, and $v = 20\ \mathrm{m\,s^{-1}}$.

6.1.2. Discharge Cycles

The discharge cycles confirm the trends observed during charge, as shown in Figures 12 and 13. Under natural convection, the temperature field remains substantially homogeneous. Under forced convection, the same vertical and in-plane gradients are reproduced, becoming more pronounced at $20\ \mathrm{m\,s^{-1}}$ and for the 2C cycle.

A notable aspect of the 2C discharge case (Figure 13) is the trade-off between maximum-temperature reduction and thermal uniformity: forced convection lowers the peak temperature but increases ΔT and σ_T compared to the natural-convection condition. This behaviour underlines that higher airflow velocities improve heat removal globally while introducing more pronounced local gradients in regions affected by edge separation and wake development.

Overall, the numerical results show a coherent thermal behaviour across all the analysed cases. Under natural convection, the temperature distribution remains nearly uniform. Under forced convection, the wall-temperature field becomes non-uniform and exhibits both vertical and horizontal gradients. The same qualitative trends are found for both charge and discharge cycles, with the 2C cases showing larger temperature differences because of the higher heat-generation rate.

The aerodynamic field is initialised before the activation of the electrochemical heat source; therefore, for a fixed inlet velocity, the initial flow topology is the same for 1C and 2C cycles. Differences between 1C and 2C appear after the thermal transient starts, because the larger current modifies the heat-generation history and the wall-temperature level. Around the voltage-drop phase of the electrical cycle, the heat-generation rate changes more rapidly and the thermal boundary layer responds through a localised increase in wall-normal temperature gradients. The velocity wake remains mainly controlled by the external geometry and by the inlet velocity, while the thermal wake is affected by the instantaneous surface-temperature distribution imposed by the battery heat release.

The flow-field interpretation is consistent with the wall-temperature maps. In natural convection, heat removal is weak and the thermal field is mostly controlled by conduction within the layered solid. In forced convection, the incoming flow accelerates around the sharp lateral edges, separates downstream of the battery, and forms a wake partially constrained by the flat plate. The central exposed regions experience stronger convective cooling, whereas edge and wake-affected regions retain higher temperatures. This explains why the forced-flow cases reduce the average temperature but increase the thermal-uniformity indices ΔT and σ_T.

It is worth making explicit the physical mechanisms that produce the observed surface-temperature patterns, since they result from the interaction of four distinct factors: the

airflow direction, the cell geometry, the heat-generation rate, and the internal thermal resistance of the layered structure. Under natural convection, the convective exchange is weak, the external flow imposes no preferential cooling, and the surface temperature is governed almost entirely by conduction inside the anisotropic layered solid. Since the in-plane conductivity of the active layers ($k_{\parallel} = 10\ \mathrm{W\,m^{-1}K^{-1}}$) is two orders of magnitude larger than the through-plane one ($k_{\perp} = 0.1\ \mathrm{W\,m^{-1}K^{-1}}$), heat spreads efficiently along the electrode planes and the resulting field is nearly uniform. Under forced convection, the picture changes qualitatively. The incoming flow accelerates around the sharp lateral edges of the prismatic cell and separates, forming a wake that is partially constrained by the downstream splitter plate. The centrally exposed portions of the lateral surface, which face the accelerated attached flow, experience the highest local convective heat-transfer coefficient and are therefore the coldest, whereas the edge regions and the wake-affected rear face, where the flow is separated and the near-wall fluid is slowly renewed, retain higher temperatures. This is the origin of the in-plane gradients. The vertical gradient has a different origin. Measurements and simulations consistently show that the wall temperature decreases monotonically with height in all the cases examined, the plane at $z = H/4$ being the warmest and the plane at $z = 7H/8$ the coolest. The drop between these two planes ranges from about 0.8 °C at 1C under natural convection to about 3 °C at 2C under forced convection. This is the behaviour expected of a wall-mounted bluff body of finite height. The free end at the top of the cell generates a downwash that entrains free-stream fluid onto the upper portion of the lateral surfaces, where the near-wall fluid is therefore continuously renewed and the local convective heat-transfer coefficient is enhanced, whereas the lower portion remains within the more sheltered part of the separated region. The effect consequently intensifies with the strength of the external flow and with the heat-generation rate, consistently with the increase of the vertical drop observed from 1C to 2C and from natural to forced convection. It is directly visible in the thermal-boundary-layer fields discussed later in this section, which show a progressive reduction of the thermal level along the z-direction. Finally, the internal thermal resistance determines how much of these externally imposed gradients survives on the surface: the low through-plane conductivity limits the redistribution of heat across the thickness and prevents the internal core from smoothing the surface non-uniformity, so the gradients imposed by the external flow are sustained rather than damped. All of these effects scale with the heat-generation rate, which is why every gradient is amplified in the 2C cycles with respect to the 1C ones, at both charge and discharge.

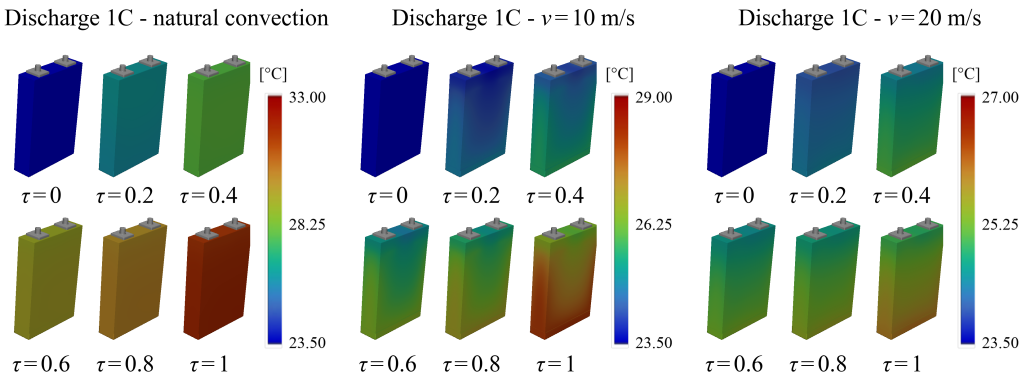

Figure 12. Wall-temperature distribution during the 1C discharge cycle. Left to right: natural convection, $v = 10\ \mathrm{m\,s^{-1}}$, and $v = 20\ \mathrm{m\,s^{-1}}$.

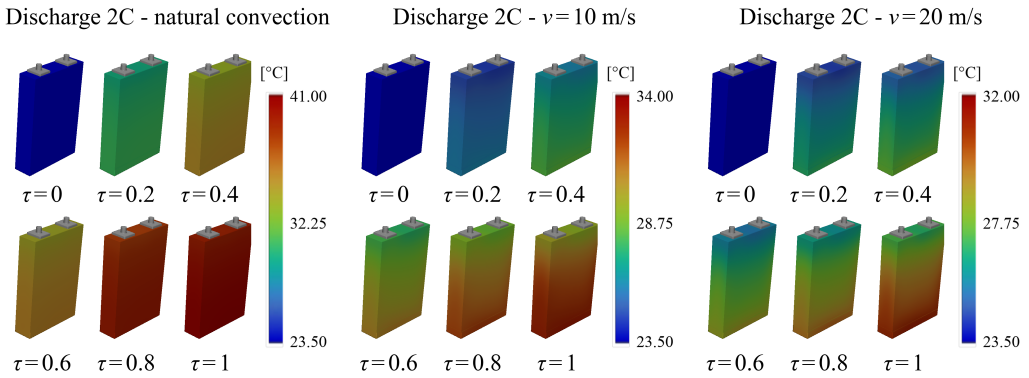

Figure 13. Wall-temperature distribution during the 2C discharge cycle. Left to right: natural convection, $v = 10\ \mathrm{m\,s^{-1}}$, and $v = 20\ \mathrm{m\,s^{-1}}$.

6.1.3. Quantitative Thermal Uniformity at End of Cycle

Tables 4 and 5 report the thermal uniformity indices at end of cycle for all cases, computed on the 28 probe locations for both CFD and EXP.

The γ index ranks the natural-convection cases as the most uniform ($\gamma > 0.973$ across all C-rates). Increasing the airflow velocity reduces γ, with the lowest values ($\gamma \approx 0.943$–0.958) reached at $20\ \mathrm{m\,s^{-1}}$ for the 2C cycle. The reference-independent index γ^* confirms this ranking for the experimental data and for the 2C numerical results; the only exception is the 1C numerical case, for which γ^* ranks the forced-convection conditions as marginally more uniform than the natural-convection one, for the reason discussed after Equation (17). In both cases, the underlying deviations are small and of comparable magnitude. The $\Delta T < 5\ ^\circ\mathrm{C}$ constraint commonly adopted in battery thermal management is satisfied by all 1C cases and by the 2C natural-convection case ($\Delta T_{\mathrm{EXP}} \leq 3.45\ ^\circ\mathrm{C}$). It is exceeded under forced convection for the 2C cycle, where the experimental spread reaches $6.42\ ^\circ\mathrm{C}$ at $10\ \mathrm{m\,s^{-1}}$ and $6.59\ ^\circ\mathrm{C}$ at $20\ \mathrm{m\,s^{-1}}$.

The σ_T values indicate a diffuse in-plane gradient rather than a localised hot spot: the central region of the lateral surface is uniformly cooler than the edges and rear face, consistent with the non-uniform convective action of the external flow. Under natural convection, σ_T remains below $1.3\ ^\circ\mathrm{C}$. Under forced convection, it grows in proportion to ΔT. Under natural convection, the CFD model predicts a larger ΔT than the experiments (e.g., 3.25 vs. $1.53\ ^\circ\mathrm{C}$ for the 1C charge case). Both indices are evaluated on the same 28 probe locations, so this discrepancy reflects a genuine difference between the simulated and measured temperature distributions, likely attributable to uncertainties in the natural-convection boundary conditions and in the electrochemical heat-generation profile at low C-rates. Charge and discharge cases show nearly identical indices at the same C-rate and velocity, confirming that thermal non-uniformity at end of cycle depends on the C-rate and aerodynamic configuration rather than on the cycle direction.

6.1.4. Thermal Boundary-Layer Evolution

The thermal boundary-layer evolution for the 2C charge case with forced convection at $v = 20\ \mathrm{m\,s^{-1}}$ is shown in Figures 14–17 at four vertical positions along the cell height. These fields confirm that the temperature gradients previously discussed from the wall-temperature maps are also reproduced in the air region surrounding the battery. Although the boundary layer separates downstream of the cell, it still contributes to heat removal from the battery surface. The lateral surface remains, on average, colder than the front and rear regions, consistently with the stronger convective action on the exposed side surfaces.

The sequence from $z = H/4$ to $z = 7H/8$ also shows a progressive reduction of the thermal level along the z-direction. This trend indicates that the near-wall air temperature field is not uniform along the battery height and that the local structure of the separated thermal boundary layer contributes to the vertical thermal gradients observed on the solid surface.

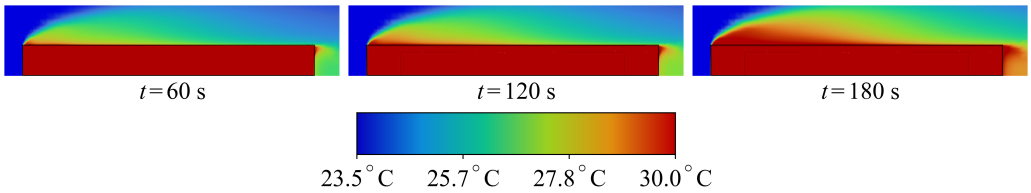

Figure 14. Thermal boundary layer evolution—Charge 2C, $v = 20\ \mathrm{m\,s^{-1}}$, at $z = H/4$.

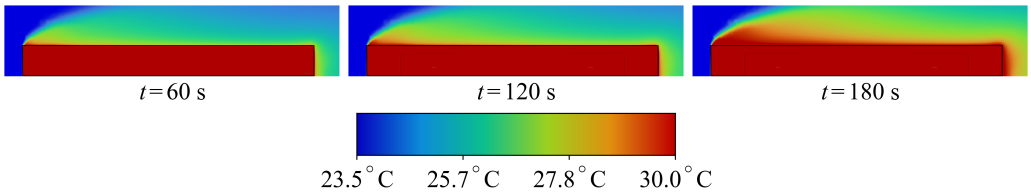

Figure 15. Thermal boundary layer evolution—Charge 2C, $v = 20\ \mathrm{m\,s^{-1}}$, at $z = H/2$.

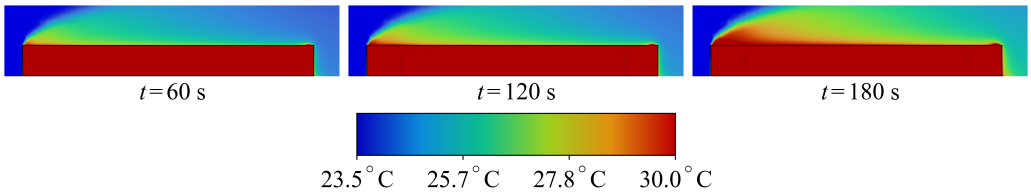

Figure 16. Thermal boundary layer evolution—Charge 2C, $v = 20\ \mathrm{m\,s^{-1}}$, at $z = 3H/4$.

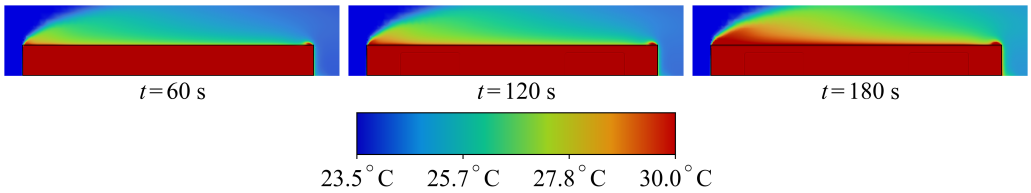

Figure 17. Thermal boundary layer evolution—Charge 2C, $v = 20\ \mathrm{m\,s^{-1}}$, at $z = 7H/8$.

6.2. Experimental Results at End of Cycle

The comparison with the experimental data is carried out by considering the end-of-cycle temperature, T_{EoC}, measured by the thermocouples located on the battery surface. In this way, the numerical and experimental datasets can be compared at the same positions and under the same operating conditions.

Figures 18 and 19 report the end-of-cycle temperature distributions measured during the charge and discharge cycles, respectively. These plots provide the experimental reference dataset used for the validation of the numerical model.

The experimental measurements confirm the same qualitative behaviour observed in the CFD+CHT simulations. Under natural convection, the temperature field is nearly uniform over the battery surface. When forced convection is imposed, the overall temperature level decreases, but the spatial distribution becomes more non-uniform. The gradients become more evident as the airflow velocity increases and are generally more pronounced for the 2C cycles, due to the larger heat-generation rate.

Figure 18 shows the measured charge cases. The 1C row exhibits moderate heating and a limited temperature spread under natural convection. The forced-flow columns show a lower average temperature but a clearer non-uniform pattern, confirming that air

cooling changes not only the heat-removal rate but also the spatial distribution of wall temperature. The 2C row shows the same trend at a higher thermal load, with larger temperature differences between the most and least cooled probe regions.

Figure 19 reports the corresponding discharge measurements. The natural-convection cases again provide the most uniform distributions, while the forced-convection cases show a stronger dependence on probe position. The comparison between the 1C and 2C rows confirms that the discharge C-rate mainly affects the thermal level and the magnitude of the gradients, whereas the spatial pattern is primarily controlled by the aerodynamic configuration.

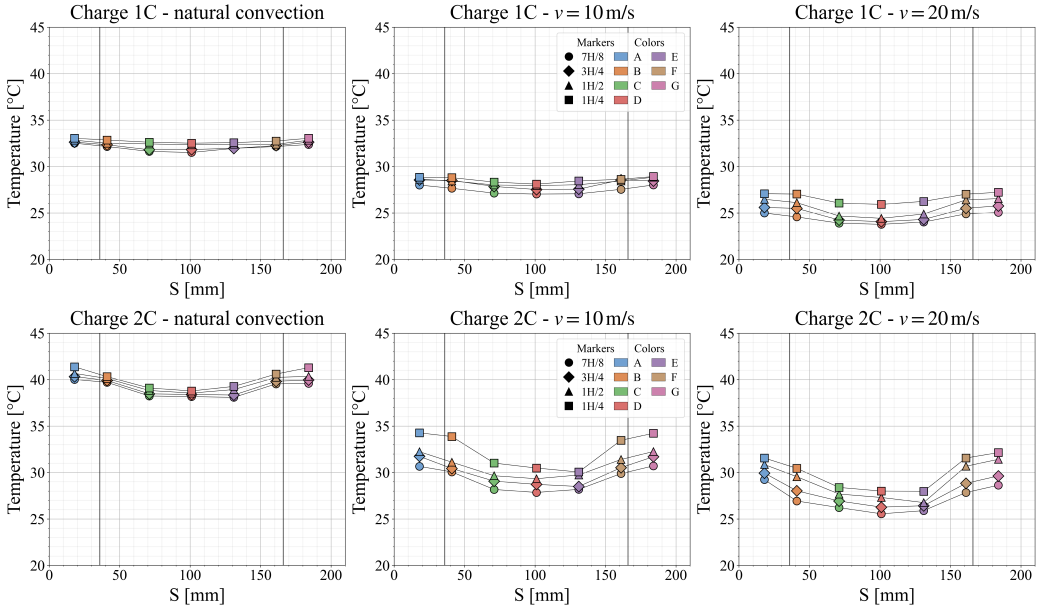

Figure 18. End-of-cycle experimental temperature measurements for the charge cycles. Top row: 1C; bottom row: 2C. Left to right: natural convection, $v = 10\ \mathrm{m\,s^{-1}}$, and $v = 20\ \mathrm{m\,s^{-1}}$.

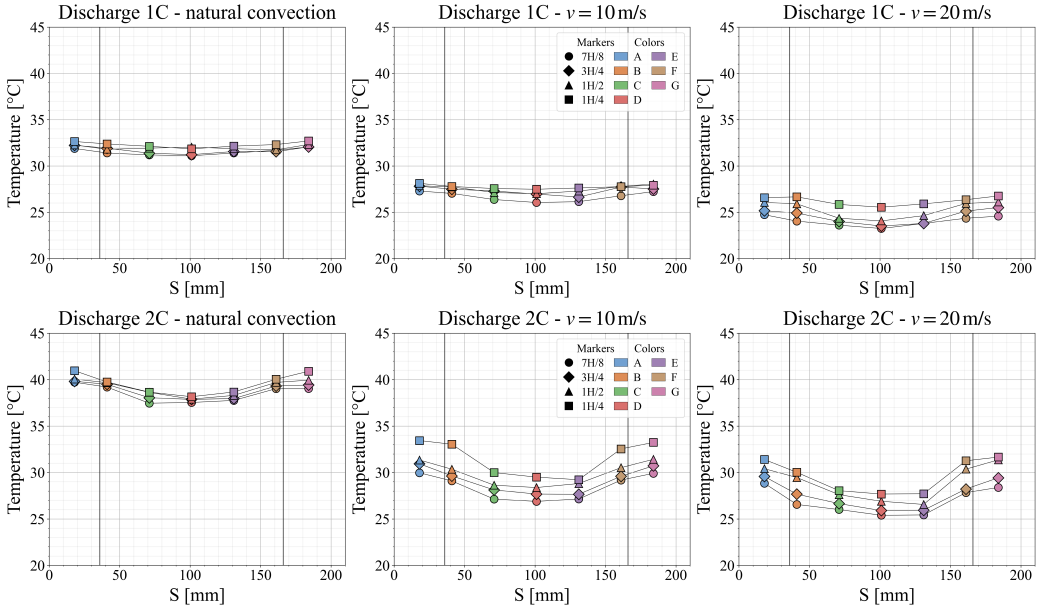

Figure 19. End-of-cycle experimental temperature measurements for the discharge cycles. Top row: 1C; bottom row: 2C. Left to right: natural convection, $v = 10\ \mathrm{m\,s^{-1}}$, and $v = 20\ \mathrm{m\,s^{-1}}$.

6.3. Comparison Between CFD and Experiments

The direct comparison between experimental measurements and CFD predictions at the end of the cycle is reported in Figure 20 for the charge cycles and in Figure 21 for the discharge cycles. In each case, the six panels cover both 1C and 2C rates under natural convection and forced convection at $v = 10\ \mathrm{m\,s^{-1}}$ and $v = 20\ \mathrm{m\,s^{-1}}$.

The error was defined as the difference between CFD and experimental measurements, so that negative values indicate an underestimation by the CFD model. The global statistics over the 168 compared thermocouple points are reported in Table 6 separately for charge and discharge. For the charge cycles, the mean bias is slightly negative (−0.277 °C), indicating a weak tendency of the CFD model to underestimate the experimental measurements. The MAE of 0.657 °C and the RMSE of 0.820 °C confirm that the deviation remains limited at the global level.

Table 6. Global error statistics for the comparison between CFD and experimental measurements, reported separately for charge and discharge cycles. The error is defined as CFD minus experimental measurements.

Metric	Charge	Discharge
Compared points	168	168
Mean bias (°C)	−0.277	−0.271
MAE (°C)	0.657	0.647
RMSE (°C)	0.820	0.811
Maximum absolute error (°C)	2.950	2.940

The error distribution depends on both C-rate and cooling condition, as summarised in Tables 7 and 8. For charge, the 2C cases show both a larger RMSE (0.910 vs. 0.719 °C) and a higher RMSE/MAE ratio (1.36 vs. 1.12) compared to the 1C cases, indicating that the larger RMSE at 2C is driven by a few points with large local deviations rather than a uniformly poorer prediction across all probes. Natural convection yields the lowest RMSE among the analysed cooling configurations (0.739 °C). The forced-convection cases show slightly larger deviations, consistent with the greater sensitivity of local heat transfer to flow separation, wake development, and the exact aerodynamic boundary conditions.

The discharge cycles show a level of agreement essentially equivalent to that of the charge cycles. The global MAE is 0.647 °C and the RMSE is 0.811 °C, with a mean bias of −0.271 °C, i.e., the same weak tendency to underestimate the measurements that is observed under charge. The maximum absolute discharge error is 2.940 °C and occurs for the 2C forced-convection case at $v = 10\ \mathrm{m\,s^{-1}}$, comparable with the maximum charge error of 2.950 °C obtained for the same operating condition. As for the charge cycles, the 2C discharge cases show larger deviations than the 1C ones (MAE 0.665 against 0.629 °C, RMSE 0.904 against 0.704 °C), and the largest deviations occur under forced convection. The agreement is remarkably symmetric between the two cycle directions: for every one of the six operating conditions, the discharge mean bias, MAE and RMSE differ from the corresponding charge values by less than 0.04 °C, which is consistent with the fact that the same aerodynamic configuration, the same heat-generation model and the same instrumentation are involved in both cases.

As observed above, although the discrepancies between the numerical and experimental results remain limited, they are consistently larger for the 2C cycles than for the 1C cycles, regardless of the cycle direction. The reasons for this behaviour cannot be fully established at this stage, and it is preferable to state explicitly what can and what cannot be concluded from the present dataset. A numerical origin can be reasonably excluded: the sensitivity studies of Section 5 and the time-step sensitivity test of Section 3.4 show that the spatial and temporal discretisation errors are at least one order of magnitude smaller than the observed deviations. What cannot be quantified with the present data are the remaining sources of

uncertainty in the CFD model, in particular the turbulence modelling, whose influence on the local convective heat-transfer coefficient is expected to be most pronounced under forced convection and in the separated and wake regions, i.e., precisely where the largest local deviations are found. Moreover, the heat-source model may be characterised by larger inaccuracies for the faster cycles: we remark that the P2D model of Lagnoni et al. [27] was adopted here without any ad hoc calibration on the present measurements, its parameters having been identified from independent electrical characterisation tests. Quantifying the impact of the above sources of uncertainty requires a dedicated uncertainty-quantification campaign outlined in Section 7, which will be the object of future studies.

Table 7. Error statistics grouped by cycle and C-rate. The error is defined as CFD minus experimental measurements. MB: mean bias.

Cycle	C-Rate	MB (°C)	MAE (°C)	RMSE (°C)
Charge	1C	−0.171	0.644	0.719
	2C	−0.383	0.670	0.910
Discharge	1C	−0.166	0.629	0.704
	2C	−0.376	0.665	0.904

Table 8. Error statistics grouped by cycle and cooling condition. The error is defined as CFD minus experimental measurements.

Cycle	Cooling Condition	MB (°C)	MAE (°C)	RMSE (°C)
Charge	Natural convection	−0.220	0.659	0.739
	Forced, 10 m s^{-1}	−0.511	0.664	0.862
	Forced, 20 m s^{-1}	−0.100	0.648	0.853
Discharge	Natural convection	−0.216	0.642	0.726
	Forced, 10 m s^{-1}	−0.498	0.649	0.853
	Forced, 20 m s^{-1}	−0.100	0.649	0.846

Figure 20 summarises the validation at the charge end-of-cycle condition. The maximum local discrepancy is reported in Table 9. The error is negative and occurs in the lower region of the geometry, showing that the largest discrepancy is localised rather than representative of a systematic offset over the full measurement domain.

Figure 21 confirms that the CFD prediction follows the experimental measurements across the whole cell surface also for the discharge cycles, with a level of agreement consistent with that obtained for the charge cycles of Figure 20.

Table 9. Largest local error observed in the CFD–experimental comparison, reported for charge and discharge separately. The two maxima occur for the same operating condition and at the same probe location.

Quantity	Charge	Discharge
Case	2C, $v = 10$ m s^{-1}	2C, $v = 10$ m s^{-1}
Location	$H/4$, $S = 41$ mm	$H/4$, $S = 41$ mm
Experimental (°C)	33.87	33.04
CFD (°C)	30.92	30.10
Error (°C)	−2.95	−2.94

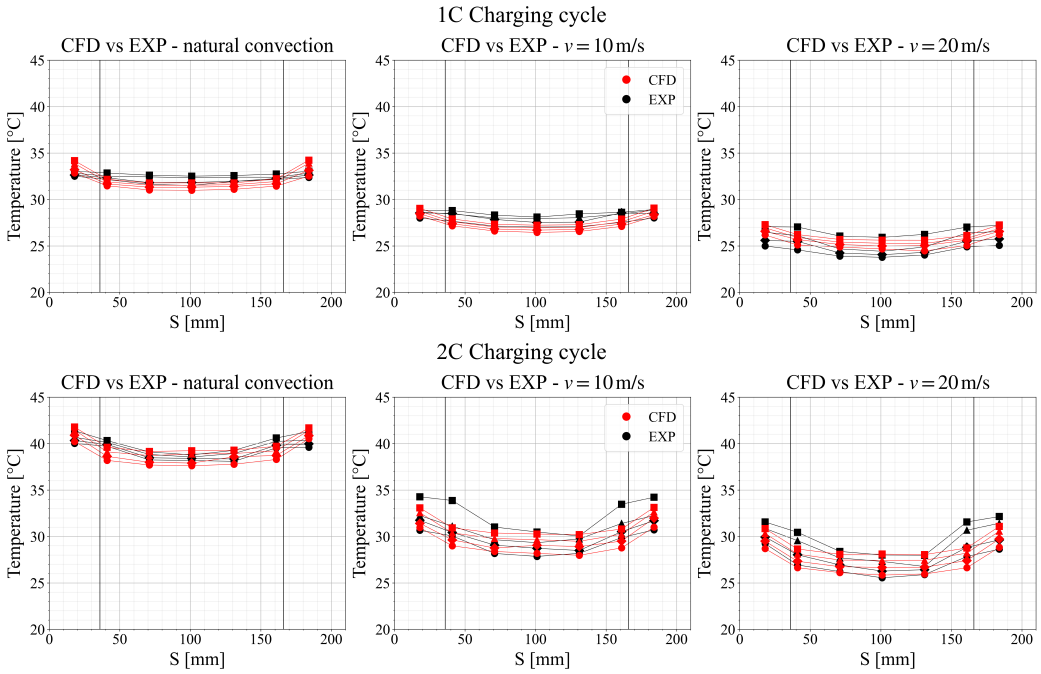

Figure 20. Comparison between experimental measurements and CFD predictions at the end of the charge cycles. Top row: 1C; bottom row: 2C. Left to right: natural convection, $v = 10\ \mathrm{m\,s^{-1}}$, and $v = 20\ \mathrm{m\,s^{-1}}$.

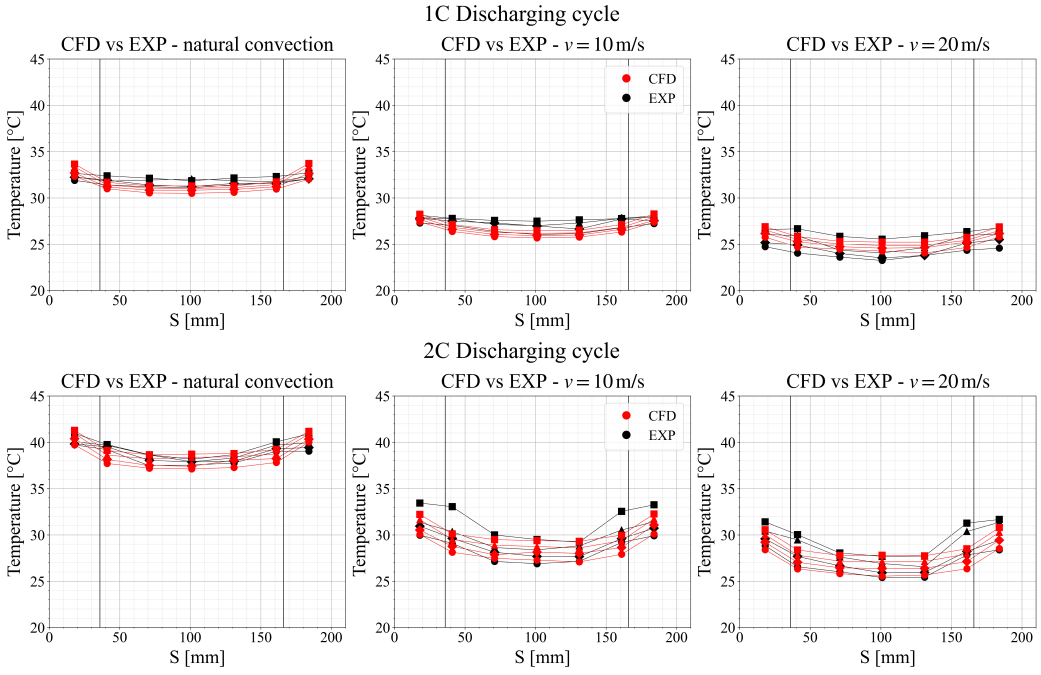

Figure 21. Comparison between experimental measurements and CFD predictions at the end of the discharge cycles. Top row: 1C; bottom row: 2C. Left to right: natural convection, $v = 10\ \mathrm{m\,s^{-1}}$, and $v = 20\ \mathrm{m\,s^{-1}}$.

7. Conclusions

In this work, a CFD+CHT methodology was developed for the thermal simulation of a commercial prismatic $LiFePO_4$ cell under different operating and cooling conditions. The approach combines a three-dimensional representation of the battery, including a simplified but physically consistent description of the internal layered structure, with

an electrochemical–thermal heat-generation model implemented in the CFD solver as a temperature- and time-dependent volumetric source term.

A dedicated numerical strategy was adopted to separate the initialisation of the external flow field from the subsequent thermal transient. First, the aerodynamic field was initialised and stabilised through steady and unsteady calculations without internal heat generation. Then, the heat source was activated within the active layers of the cell and updated during the transient simulation according to the local temperature and to the evolution of the state of charge. This procedure allowed the full thermal response of the battery to be simulated with a computational cost compatible with future extensions to larger battery assemblies.

The numerical results showed that the wall-temperature evolution is approximately monotonic for both 1C and 2C cycles. Under natural convection, the temperature field remains substantially uniform over the battery surface, indicating that the thermal behaviour is mainly governed by internal conduction and weak convective exchange with the surrounding air. Under forced convection, the surface temperature becomes more non-uniform and exhibits both vertical and in-plane gradients. These effects become more pronounced as the airflow velocity increases from 10 $\mathrm{m\,s^{-1}}$ to 20 $\mathrm{m\,s^{-1}}$, and are further enhanced in the 2C cycle because of the higher heat-generation rate.

The methodology was validated through a dedicated experimental campaign carried out in the wind tunnel of the University of Pisa. The same prismatic cell was instrumented with type-K thermocouples distributed over its external surfaces, and the thermal measurements were acquired under operating conditions consistent with those reproduced numerically. The experimental and CFD cases were compared at the same reference ambient temperature, all the tests having been carried out within a 22.5–24.5 °C window and normalised to 23.5 °C, so that the validation focused on the heat-generation and heat-transfer modelling rather than on differences in initial or boundary temperature. The comparison between CFD predictions and experimental measurements was performed at the thermocouple locations, focusing on the end-of-cycle wall-temperature distribution.

The quantitative validation, summarised in Tables 6–9, showed that the CFD model reproduces the overall thermal level measured experimentally. For the charge cycles, the MAE is 0.657 °C, the RMSE is 0.820 °C, and the mean bias is −0.277 °C. The negative bias indicates a weak tendency to underestimate the experimental measurements. The 2C cases showed a larger RMSE and a higher RMSE/MAE ratio than the 1C cases, indicating that the larger error at 2C is driven by a few points with large local deviations rather than a uniformly poorer prediction. Natural convection yielded the lowest RMSE among the analysed cooling configurations. For the discharge cycles, the agreement is essentially equivalent, with an MAE of 0.647 °C, an RMSE of 0.811 °C and a mean bias of −0.271 °C, showing that the methodology is equally predictive for both cycle directions.

The maximum absolute charge error was 2.950 °C, occurring for the 2C case with forced convection at $v = 10\ \mathrm{m\,s^{-1}}$, where the CFD value was 30.92 °C against an experimental measurement of 33.87 °C. For the discharge cycles, the maximum absolute error was 2.940 °C, occurring for the same operating condition. In both cases, the largest discrepancies are localised and do not correspond to a systematic error over the whole domain. These deviations therefore exceed the approximately ±1 °C absolute accuracy of the measurement chain, and should consequently be interpreted as actual differences between the numerical prediction and the experimental measurements rather than as deviations falling within the experimental uncertainty. They should be considered together with the substantially lower global error statistics reported above. The experimental characterisation further showed a channel-to-channel consistency of approximately ±0.1 °C after the initial offset correction and an end-of-cycle repeatability within ±0.2 °C over three repetitions. These

quantities characterise different aspects of the measurement procedure and should not be directly compared with the CFD–experiment discrepancy. The residual deviations, larger for the 2C cycles than for the 1C ones for both charge and discharge, cannot be attributed to a single identified cause with the present dataset: numerical discretisation has been shown to be negligible, while turbulence modelling and the accuracy of the heat-generation model at high C-rates remain unquantified. A future uncertainty-quantification activity will be required to separate the contributions associated with turbulence modelling, ambient-temperature control, electrical-current measurement, the effective thermal properties, including the through-plane conductivity, the electrochemical heat-generation model, and CFD discretisation.

Nonetheless, the developed approach represents a reliable and extensible basis for the thermal analysis of prismatic lithium-ion cells and provides a scalable framework for future applications to battery modules and full battery packs. Future developments will focus on extending the methodology to multi-cell configurations, including more complex cooling layouts, dynamic operating cycles representative of real automotive applications, and uncertainty-aware validation procedures. As an immediate next step, a dedicated uncertainty-quantification campaign will be conducted to assess the sensitivity of the predicted temperature field to the internal thermal conductivities of the active and passive layers, whose influence on the overall thermal response has not yet been systematically characterised.

Author Contributions: Conceptualization, A.B., G.L., M.V.S. and A.M.; Methodology, D.F., M.L., C.S., F.G.Q., A.B., G.L., M.V.S. and A.M.; Software, D.F. and F.F.; Formal analysis, A.B., G.L., M.V.S. and A.M.; Investigation, D.F., M.L., C.S., F.G.Q.; Data curation, D.F., M.L., C.S., F.G.Q. and F.F.; Writing—original draft, D.F., M.L., C.S., F.G.Q. and F.F.; Writing—review & editing, A.B., G.L., M.V.S. and A.M.; Visualization, D.F.; Supervision, A.B., G.L., M.V.S. and A.M. All authors have read and agreed to the published version of the manuscript.

Funding: This research was funded by MOST—Sustainable Mobility Center through European Union Next-GenerationEU (Piano Nazionale di Ripresa e Resilienza (PNRR)—MISSIONE 4, COMPONENTE 2, INVESTIMENTO 1.4—D.D.1033 17 June 2022, CN00000023). M.L. and A.B. acknowledge funding from the European Union NextGeneration EU—National Recovery and Resilience Plan (NRRP)—MISSION 4 Component 2, INVESTMENT N. 1.3—CUP N. I53C22001450006, within the Project 'Network 4 Energy Sustainable Transition (NEST).

Institutional Review Board Statement: Not applicable.

Informed Consent Statement: Not applicable.

Data Availability Statement: The data presented in this study are available on request from the author (duccio.fedeli@phd.unipi.it).

Conflicts of Interest: The authors declare no conflicts of interest.

References

1. Bandhauer, T.M.; Garimella, S.; Fuller, T.F. A Critical Review of Thermal Issues in Lithium-Ion Batteries. *J. Electrochem. Soc.* **2011**, *158*, R1–R25. [CrossRef]
2. Alipour, M.; Ziebert, C.; Conte, F.V.; Kizilel, R. A Review on Temperature-Dependent Electrochemical Properties, Aging, and Performance of Lithium-Ion Cells. *Batteries* **2020**, *6*, 35. [CrossRef]
3. Lin, J.; Liu, X.; Li, S.; Zhang, C.; Yang, S. A review on recent progress, challenges and perspective of battery thermal management system. *Int. J. Heat Mass Transf.* **2021**, *167*, 120834. [CrossRef]
4. Zhang, X.; Li, Z.; Luo, L.; Fan, Y.; Du, Z. A review on thermal management of lithium-ion batteries for electric vehicles. *Energy* **2022**, *238*, 121652. [CrossRef]
5. Olabi, A.G.; Maghrabie, H.M.; Adhari, O.H.K.; Sayed, E.T.; Yousef, B.A.A.; Salameh, T.; Kamil, M.; Abdelkareem, M.A. Battery thermal management systems: Recent progress and challenges. *Int. J. Thermofluids* **2022**, *15*, 100171. [CrossRef]

6. Liu, S.; Zhang, G.; Wang, C.Y. Challenges and Innovations of Lithium-Ion Battery Thermal Management Under Extreme Conditions: A Review. *J. Heat Mass Transf.* **2023**, *145*, 080801. [CrossRef]
7. Gharehghani, A.; Rabiei, M.; Mehranfar, S.; Saeedipour, S.; Mahmoudzadeh Andwari, A.; García, A.; Reche, C.M. Progress in battery thermal management systems technologies for electric vehicles. *Renew. Sustain. Energy Rev.* **2024**, *202*, 114654. [CrossRef]
8. Hwang, F.S.; Confrey, T.; Reidy, C.; Picovici, D.; Callaghan, D.; Culliton, D.; Nolan, C. Review of Battery Thermal Management Systems in Electric Vehicles. *Renew. Sustain. Energy Rev.* **2024**, *192*, 114171. [CrossRef]
9. Wang, Z.; Du, C. A Comprehensive Review on Thermal Management Systems for Power Lithium-Ion Batteries. *Renew. Sustain. Energy Rev.* **2021**, *139*, 110685. [CrossRef]
10. Bernardi, D.; Pawlikowski, E.; Newman, J. A General Energy Balance for Battery Systems. *J. Electrochem. Soc.* **1985**, *132*, 5–12. [CrossRef]
11. Forgez, C.; Vinh Do, D.; Friedrich, G.; Morcrette, M.; Delacourt, C. Thermal modeling of a cylindrical $LiFePO_4$/graphite lithium-ion battery. *J. Power Sources* **2010**, *195*, 2961–2968. [CrossRef]
12. Prada, E.; Di Domenico, D.; Creff, Y.; Bernard, J.; Sauvant-Moynot, V.; Huet, F. Simplified Electrochemical and Thermal Model of $LiFePO_4$-Graphite Li-Ion Batteries for Fast Charge Applications. *J. Electrochem. Soc.* **2012**, *159*, A1508–A1519. [CrossRef]
13. Kleiner, J.; Komsiyska, L.; Elger, G.; Endisch, C. Thermal Modelling of a Prismatic Lithium-Ion Cell in a Battery Electric Vehicle Environment: Influences of the Experimental Validation Setup. *Energies* **2020**, *13*, 62. [CrossRef]
14. Smith, K.A.; Rahn, C.D.; Wang, C.Y. Control oriented 1D electrochemical model of lithium ion battery. *Energy Convers. Manag.* **2007**, *48*, 2565–2578. [CrossRef]
15. Smith, K.A.; Rahn, C.D.; Wang, C.Y. Model Order Reduction of 1D Diffusion Systems via Residue Grouping. *J. Dyn. Syst. Meas. Control* **2008**, *130*, 011012. [CrossRef]
16. Guo, M.; Sikha, G.; White, R.E. Single-Particle Model for a Lithium-Ion Cell: Thermal Behavior. *J. Electrochem. Soc.* **2011**, *158*, A122–A132. [CrossRef]
17. Dao, T.S.; Vyasarayani, C.P.; McPhee, J. Simplification and order reduction of lithium-ion battery model based on porous-electrode theory. *J. Power Sources* **2012**, *198*, 329–337. [CrossRef]
18. Hu, X.; Li, S.; Peng, H. A comparative study of equivalent circuit models for Li-ion batteries. *J. Power Sources* **2012**, *198*, 359–367. [CrossRef]
19. Xu, Z.; Xu, J.; Guo, Z.; Wang, H.; Sun, Z.; Mei, X. Design and Optimization of a Novel Microchannel Battery Thermal Management System Based on Digital Twin. *Energies* **2022**, *15*, 1421. [CrossRef]
20. Kapteyn, M.G.; Knezevic, D.J.; Huynh, D.B.P.; Tran, M.; Willcox, K.E. Data-driven physics-based digital twins via a library of component-based reduced-order models. *Int. J. Numer. Methods Eng.* **2022**, *123*, 2986–3003. [CrossRef]
21. Subramani, T.; Bartscher, S. Predictive Digital Twins for Thermal Management Using Machine Learning and Reduced-Order Models. *arXiv* **2025**, arXiv:2505.06849.
22. Panchal, S.; Dincer, I.; Agelin-Chaab, M.; Fraser, R.; Fowler, M. Transient electrochemical heat transfer modeling and experimental validation of a large sized $LiFePO_4$/graphite battery. *Int. J. Heat Mass Transf.* **2017**, *109*, 1239–1251. [CrossRef]
23. Wang, T.; Tseng, K.J.; Zhao, J.; Wei, Z. Thermal investigation of lithium-ion battery module with different cell arrangement structures and forced air-cooling strategies. *Appl. Energy* **2014**, *134*, 229–238. [CrossRef]
24. Chen, D.; Jiang, J.; Kim, G.H.; Yang, C.; Pesaran, A. Comparison of different cooling methods for lithium ion battery cells. *Appl. Therm. Eng.* **2016**, *94*, 846–854. [CrossRef]
25. Akbarzadeh, M.; Kalogiannis, T.; Jaguemont, J.; He, J.; Jin, L.; Berecibar, M.; Van Mierlo, J. Thermal modeling of a high-energy prismatic lithium-ion battery cell and module based on a new thermal characterization methodology. *J. Energy Storage* **2020**, *32*, 101707. [CrossRef]
26. Kong, D.; Wang, G.; Ping, P.; Wen, J.X. A coupled conjugate heat transfer and CFD model for the thermal runaway evolution and jet fire of 18650 lithium-ion battery under thermal abuse. *eTransportation* **2022**, *12*, 100157. [CrossRef]
27. Lagnoni, M.; Scarpelli, C.; Lutzemberger, G.; Bertei, A. Critical Comparison of Equivalent Circuit and Physics-Based Models for Lithium-Ion Batteries: A Graphite/Lithium-Iron-Phosphate Case Study. *J. Energy Storage* **2024**, *94*, 112326. [CrossRef]
28. GWL Power. ZG-LFP060AH Technical Specification. 2025. Available online: https://files.gwl.eu/inc/_doc/attach/StoItem/4091/ZG-LFP060AHA_datasheet.pdf (accessed on 7 May 2026).
29. Barbieri, M.; Ceraolo, M.; Lutzemberger, G.; Scarpelli, C. An Electro–Thermal Model for LFP Cells: Calibration Procedure and Validation. *Energies* **2022**, *15*, 2653. [CrossRef]
30. Igbalajobi, A.; McClean, J.F.; Sumner, D.; Bergstrom, D.J. The effect of a wake-mounted splitter plate on the flow around a surface-mounted finite-height circular cylinder. *J. Fluids Struct.* **2013**, *37*, 185–200. [CrossRef]
31. Ogunremi, A.R.; Sumner, D. The effect of a splitter plate on the flow around a finite prism. *J. Fluids Struct.* **2015**, *59*, 1–21. [CrossRef]
32. Nakamura, Y.; Ohya, Y.; Tsuruta, H. Experiments on vortex shedding from flat plates with square leading and trailing edges. *J. Fluid Mech.* **1991**, *222*, 437–447. [CrossRef]

33. Rastan, M.R.; Shahbazi, H.; Sohankar, A.; Alam, M.M.; Zhou, Y. The wake of a wall-mounted rectangular cylinder: Cross-sectional aspect ratio effect. *J. Wind Eng. Ind. Aerodyn.* **2021**, *213*, 104615. [CrossRef]
34. Jokar, A.; Rajabloo, B.; Désilets, M.; Lacroix, M. Review of simplified Pseudo-two-Dimensional models of lithium-ion batteries. *J. Power Sources* **2016**, *327*, 44–55. [CrossRef]
35. Steinhardt, M.; Gillich, E.I.; Stiegler, M.; Jossen, A. Thermal conductivity inside prismatic lithium-ion cells with dependencies on temperature and external compression pressure. *J. Energy Storage* **2020**, *32*, 101680. [CrossRef]
36. Lagnoni, M.; Nicolella, C.; Bertei, A. Survey and sensitivity analysis of critical parameters in lithium-ion battery thermo-electrochemical modeling. *Electrochim. Acta* **2021**, *394*, 139098. [CrossRef]
37. Preston-Thomas, H. The International Temperature Scale of 1990 (ITS-90). *Metrologia* **1990**, *27*, 3–10. [CrossRef]
38. *IEC 60584-1:2013*; Thermocouples—Part 1: EMF Specifications and Tolerances. International Electrotechnical Commission (IEC): Geneva, Switzerland, 2013.
39. National Instruments. *NI 9219 Datasheet—4-Channel, 24-Bit Universal Analog Input Module*; National Instruments Corp.: Austin, TX, USA, 2016.
40. Wang, Y.; Zhang, X.; Chen, Z. Experimental study on the effect of ambient temperature and discharge rate on the temperature field of prismatic batteries. *J. Energy Storage* **2023**, *59*, 106577. [CrossRef]
41. Li, J.; Sun, D.; Jin, X.; Shi, W.; Sun, C. Influence of Different Ambient Temperatures on the Discharge Performance of Square Ternary Lithium-Ion Batteries. *Energies* **2022**, *15*, 5348. [CrossRef]
42. Weltens, H.; Bressler, H.; Terres, F.; Neumaier, H.; Rammoser, D. Optimisation of Catalytic Converter Gas Flow Distribution by CFD Prediction. In *Proceedings of the SAE Technical Paper*; SAE International: Warrendale, PA, USA, 1993; p. 930780. [CrossRef] [PubMed]